

Probing Heavy Axion-like Particles from Massive Stars with X -rays and Gamma Rays

James H. Buckley^{a,*}, P. S. Bhupal Dev^{a,†}, Francesc Ferrer^{a,‡} and Takuya Okawa^{a,b,§}

^a *Department of Physics and McDonnell Center for the Space Sciences,
Washington University, Saint Louis, MO 63130, USA and*

^b *Theoretical Physics Department, Fermi National Accelerator Laboratory, Batavia, IL 60510, USA*

(Dated: December 31, 2024)

The hot interiors of massive stars in the later stages of their evolution provide an ideal place for the production of heavy axion-like particles (ALPs) with mass up to $\mathcal{O}(100 \text{ keV})$ range. We show that a fraction of these ALPs could stream out of the stellar photosphere and subsequently decay into two photons that can be potentially detected on or near the Earth. In particular, we estimate the photon flux originating from the spontaneous decay of heavy ALPs produced inside Horizontal Branch and Wolf-Rayet stars, and assess its detectability by current and future X -ray and gamma-ray telescopes. Our results indicate that current and future telescopes can probe axion-photon couplings down to $g_{a\gamma} \sim 4 \times 10^{-11} \text{ GeV}^{-1}$ for $m_a \sim 10 - 100 \text{ keV}$, which covers new ground in the ALP parameter space.

I. INTRODUCTION

The QCD axion is the pseudo Nambu-Goldstone (pNGB) boson associated with the Peccei-Quinn (PQ) symmetry, that provides an elegant solution to the strong CP problem [1–3] and can also account for the dark matter in the Universe [4–6]. More generally, axion-like-particles (ALPs) appear as pNGBs in theories with a spontaneously broken global $U(1)$ symmetry unrelated to the PQ mechanism, and are ubiquitous in string-inspired extensions of the Standard Model (SM) [7, 8]. ALPs are predicted to have interactions with SM particles analogous to those of QCD axions, but the latter are restricted to couple in inverse proportion to their mass, whereas the ALP mass and couplings can be treated as independent parameters. The ALP parameter space is being probed by numerous laboratory and astrophysical searches [9].

The original QCD axion had a keV–MeV mass and electroweak scale interactions. It was soon experimentally ruled out [10], leading to the emergence of *invisible* QCD axion models [11–16]. Although the QCD axion that addresses the strong CP problem is predicted to have a mass lighter than $\lesssim \text{eV}$, ‘heavy’ ALPs appear in many ultraviolet (UV) completions of the SM [17], e.g. as decay products of dark matter candidates [18].

Interestingly, heavy axions with masses $m_a \gtrsim \mathcal{O}(10 \text{ keV})$ can have lifetimes τ_a comparable to the age of the Universe $t_U \sim 4 \times 10^{17} \text{ s}$, i.e.

$$\tau_a = \frac{64\pi}{g_{a\gamma}^2 m_a^3} \simeq 10^{17} \text{ s} \left(\frac{10^{-12} \text{ GeV}^{-1}}{g_{a\gamma}} \right)^2 \left(\frac{10 \text{ keV}}{m_a} \right)^3, \quad (1)$$

where $g_{a\gamma}$ is the axion-photon coupling that induces the $a \rightarrow \gamma\gamma$ decay. Thus, if produced in the late Universe,

heavy ALPs typically decay on timescales shorter than the age of the Universe and could give rise to detectable photon signals. For this reason, we will focus on ALPs with masses in the range from keV to MeV.

The axion-photon coupling $g_{a\gamma}$ for ALPs in this mass range is constrained by cosmological observations, high energy experiments, as well as astrophysical phenomena. In the context of cosmology, ALPs decaying to photons in the early Universe affect cosmological observables in a model-dependent way, impacting Big-Bang Nucleosynthesis (BBN) and distortions of the Cosmic Microwave Background (CMB) radiation spectrum. ALPs can be produced thermally, by the decay of heavier particles or from topological defects such as cosmic strings and domain walls, or from primordial black holes via the Hawking evaporation process. The injection of their decay products into the thermal bath of the early Universe modifies the abundances of nuclei such as Deuterium and Helium-4, and it can also induce distortions of the CMB spectrum [19–21]. Moreover, heavy ALPs could be produced at colliders: they give rise to the process $e^+e^- \rightarrow \gamma^* \rightarrow \gamma + a$ at LEP [22] and the radiative up-silon decay $\Upsilon \rightarrow \gamma^* \rightarrow \gamma + a$ at the Crystal Ball [23], BaBar [24] and Belle [25] experiments. Limits on ALPs from radiative Z -boson decays were obtained by the L3 collaboration [26] and, more recently, by the ATLAS experiment [27]. In addition, electron beam dump experiments including E141 and E137 [28, 29], as well as proton beam dump experiments such as CHARM [30] and NuCal [31, 32] are effective in probing such heavy ALPs.

Heavy ALPs would also be copiously produced in hot and dense astrophysical environments. ALPs produced in supernovae could contribute significantly to energy loss [33], may produce a large flux of photons from decays that could be detected by telescopes [34–38], or can contribute to the energetics of expanding supernovae [39]. ALPs could also be produced in main sequence (MS) stars [40], horizontal branch (HB) stars [41–43], Wolf-Rayet (WR) stars [44], neutron stars [45] and neutron star mergers [46, 47].

In this paper, we consider the production of heavy

* buckley@wustl.edu

† bdev@wustl.edu

‡ ferrer@wustl.edu

§ o.takuya@wustl.edu

ALPs with $m_a \simeq (10 - 100)$ keV in HB stars and WR stars which have high enough core temperatures to produce these particles. An HB star consists of a Helium-burning core and a Hydrogen-burning shell. Stars reach the horizontal branch after leaving the MS and going through a red giant phase. On the other hand, WR stars [48] are massive stars whose outer envelopes are stripped away because of their high rotational speeds. Such stars are also likely to have Helium-burning layers that reach temperatures of $\mathcal{O}(10)$ keV (or 10^8 K), which is about ten times larger than that of MS stars, and are conducive for the production of heavy ALPs. ALPs produced in the plasma of such stars undergo decays to two photons that might be observable by telescopes on Earth unless the decay occurs inside the photosphere of the star. Previous studies searching for axions produced inside HB stars or WR stars looked for the effect of the star's energy loss [41–43] or X -rays converted from light axions [44]. In this paper, we focus on the decaying heavy ALP scenario, and estimate the flux of photons from decays of heavy ALPs produced in HB stars in two globular clusters, i.e. NGC 6397 and NGC 2808, and that from WR stars in the Quintuplet Cluster. These particular sources are chosen based on the distance from the Earth (closer is better) and the number of HB stars (more is better). We then discuss their detectability at future X -ray/gamma-ray telescopes.

The paper is structured as follows. Sec. II briefly summarizes the production mechanisms of heavy axions inside stars. The flux of photons at the Earth from their decay is estimated in Sec. III, which also includes a description of the reach of X -ray/gamma-ray telescopes and the expected background. Finally, the results and conclusions can be found in Sec. IV and Sec. V, respectively. A detailed description of the modeling of WR stars is provided in Appendix A.

II. ALP PRODUCTION IN PLASMA

Here we focus on signals that are caused by the interaction of ALPs with the electromagnetic field. This is encoded in the following term in the Lagrangian density:

$$\mathcal{L}_{a\gamma} = -\frac{g_{a\gamma}}{4} F_{\mu\nu} \tilde{F}^{\mu\nu} a, \quad (2)$$

where $g_{a\gamma}$ is the ALP-photon coupling, which is taken to be independent of the mass of the ALP field a ; $F_{\mu\nu}$ is the electromagnetic field-strength tensor, and $\tilde{F}_{\mu\nu}$ is its dual. This interaction term leads to the production of axions in stars via two processes: (i) the Primakoff process [19, 42, 49, 50] $\gamma + Ze \rightarrow Ze + a$, in which a photon is converted into an axion in the electrostatic field of charged particles in the plasma, and (ii) photon coalescence [35, 39, 51] $\gamma + \gamma \rightarrow a$ where two photons in the plasma annihilate into one axion. Production rates of axions by these processes have different dependence on the axion mass m_a and the plasma temperature T . In the

interior of HB and WR stars, with temperatures reaching $T \sim 10^8$ K, axions with mass up to $m_a \lesssim 50$ keV are more efficiently produced by the Primakoff process. In contrast, those with higher masses, $m_a \gtrsim 50$ keV, are mostly produced by photon coalescence [42]. We do not consider other interaction terms (e.g. axion-electron or axion-nucleon coupling), and their associated production processes, which could in principle enhance the detection prospects discussed here.

In the following, the production spectra (i.e. the number density of axions produced per unit time and frequency) from the Primakoff process and photon coalescence are summarized. The momentum of each particle is labeled as in Fig. 1. In the following, we have only considered the two transverse modes of the photon, which follow the dispersion relation $\omega^2 = k^2 + \omega_{\text{pl}}^2$. Here k is the momentum of a photon, ω is the frequency of a photon, and ω_{pl} is the plasma frequency. See Sec. II C for a discussion of the longitudinal mode contribution.

A. Primakoff Process

Photons, electrons, and ionized nuclei are in thermal equilibrium in the core of a star. The motion of this plasma induces strong magnetic fields that could convert a photon in the stellar plasma into an axion by the Primakoff process $\gamma(k) + Ze^-(k') \rightarrow a(p) + Ze^-(p')$. Here $k^\mu = (E_\gamma, \mathbf{k})$ is the four-momentum of the incoming photon, $p = (E_a, \mathbf{p})$ is that of the outgoing axion, $k' = (E_e, \mathbf{k}')$ is that of the incoming electron/nucleus with atomic number Z , $p' = (E'_e, \mathbf{p}')$ is that of the outgoing nucleus, and $q \equiv p - k = k' - p'$ is the momentum transfer.

The invariant matrix of this process is given by

$$-i\mathcal{M} = \bar{u}(p')(iZe\gamma^\alpha)u(k') \frac{-i\eta_{\alpha\nu}}{q^2} (-ig_{a\gamma})\epsilon_\mu(k)k_\rho q_\sigma \epsilon^{\mu\nu\rho\sigma}, \quad (3)$$

where $\eta^{\mu\nu}$ is the metric in the Minkowski space and $\epsilon^{\mu\nu\rho\sigma}$ is a totally anti-symmetric tensor. Since the plasma temperature of stars $T \simeq \mathcal{O}(10 \text{ keV})$ is typically much lower than nucleus mass $m_N \gtrsim \mathcal{O}(1 \text{ GeV})$, we could safely approximate that (i) the nuclei are at rest in the rest frame of the star's plasma and (ii) the recoil of the nucleus involved in the Primakoff process is negligible. Correspondingly, we approximate $q^\mu \approx (0, \mathbf{q})$ and $k'^\mu, p'^\mu \approx (m_N, \mathbf{0})$. Under these assumptions, the squared invariant amplitude, averaged over the initial two transverse modes of the photon and two spin states of the nucleus, and summed over the final two spin states of the nucleus, is given by

$$\langle |\mathcal{M}|^2 \rangle = \frac{8\pi g_{a\gamma}^2 Z^2 \alpha m_e^2}{q^2} [|\mathbf{k}|^2 |\mathbf{p}|^2 - (\mathbf{k} \cdot \mathbf{p})^2], \quad (4)$$

where $\alpha = e^2/4\pi$ is the fine-structure constant. The polarization sum of photons is evaluated as $\sum \epsilon_\alpha^* \epsilon_\beta =$

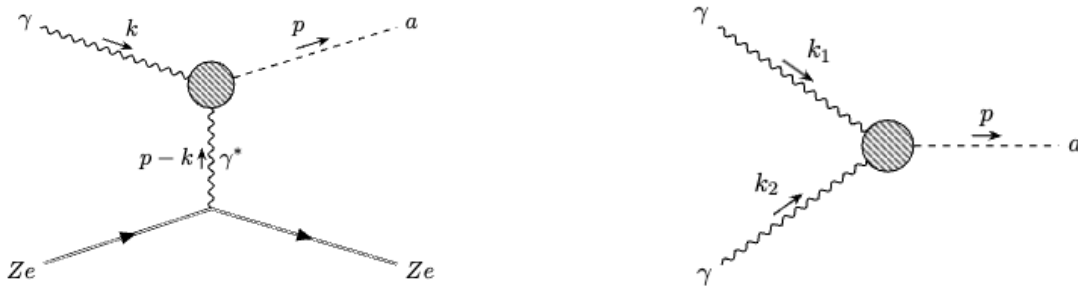


Figure 1: Two main processes considered here that can efficiently produce axions in the stellar core: the Primakoff process (left) and photon coalescence (right).

$-\eta_{\alpha\beta}$. The production spectrum of the Primakoff process is then expressed as:

$$\begin{aligned} \frac{dn_a}{dt} = & g_\gamma g_N \int \frac{d^3\mathbf{k}}{(2\pi)^3 2E_\gamma} f_B(E_\gamma) \int \frac{d^3\mathbf{k}'}{(2\pi)^3 2m_N} f_{B/F}(E_{k'}) \\ & \times \int \frac{d^3\mathbf{p}}{(2\pi)^3 2E_a} \int \frac{d^3\mathbf{p}'}{(2\pi)^3 2m_N} (1 \pm f_{B/F}(E_{p'})) \\ & \times (2\pi)^4 \delta(E_\gamma - E_a) \delta^{(3)}(\mathbf{k}' - \mathbf{p}') \frac{1}{S} \langle |\mathcal{M}|^2 \rangle. \end{aligned} \quad (5)$$

Here, $E_\gamma = \sqrt{k^2 + \omega_{\text{pl}}^2}$ is the photon energy, $\omega_{\text{pl}} \simeq 4\pi\alpha n_e/m_e$ is the plasma frequency, g_i is the number of degrees of freedom of particle i , $f_{B/F} = 1/(e^{(E-\mu)/T} \mp 1)$ denotes the Bose/Fermi distribution, and $S = 1$ is the symmetry factor. We neglect the Bose enhancement due to axions as their occupation number is quite low; $f_a \ll 1$. In a plasma, the electric field is effectively shielded because charged particles tend to be surrounded by an oppositely charged cloud. To include this screening effect, we follow the formalism suggested in Ref. [52] where the factor $1/q^4$ in $\langle |\mathcal{M}|^2 \rangle$ is replaced by $1/(q^2(q^2 + \kappa^2))$. Here κ is the screening scale or the inverse of the Debye length λ_D , which measures the effectiveness of screening of electric fields by charged particles in the plasma. Using the Debye-Huckel approximation, the screening scale κ is found as

$$\kappa^2 = \frac{4\pi\alpha}{T} \left(n_e^{\text{eff}} + \sum_j Z_j^2 n_j^{\text{eff}} \right) \quad (6)$$

in a nondegenerate medium. Here n_j^{eff} is the effective number density:

$$n_j^{\text{eff}} = g_j \int \frac{d^3\mathbf{p}}{(2\pi)^3} f_{B/F}(1 \pm f_{B/F}), \quad (7)$$

of a particle with a charge $Z_j e$ and degeneracy g_j . Note that this replacement allows us to reproduce the form factor of the charge distribution of the plasma that consists of charged particles following the Yukawa potential $V = \frac{Z_e}{4\pi\epsilon_0 r} e^{-\kappa r}$ in the limit of negligible recoil of electrons/nuclei.

The environment of our interest consists not only of electrons but of other ionized nuclei; the core of HB stars contains ^1H and ^4He and that of WR stars in the WC phase also have heavier nuclei such as ^{12}C . In order to take into account contributions from all of these nuclei, we assume that the total Primakoff production rate can be obtained by summing Eq. (5) over all kinds of target nuclei:

$$\left. \frac{dn_a}{dt} \right|_{\text{total}} = \sum_{\text{ions, electrons}} \left. \frac{dn_a}{dt} \right|_{\text{ions, electrons}}. \quad (8)$$

Taking a derivative with respect to E_a and performing integrations, we finally obtain the Primakoff production spectrum:

$$\begin{aligned} \frac{d^2 n_a}{dE_a dt} (T(r), \kappa(r), t, E_a) = & \frac{g_{a\gamma}^2 T \kappa^2}{32\pi^3} p k f_B(E_\gamma) \\ & \times \left\{ \frac{[(k+p)^2 + \kappa^2][(k-p)^2 + \kappa^2]}{4pk\kappa^2} \ln \left[\frac{(k+p)^2 + \kappa^2}{(k-p)^2 + \kappa^2} \right] \right. \\ & \left. - \frac{(k^2 - p^2)^2}{4kp\kappa^2} \ln \left[\frac{(k+p)^2}{(k-p)^2} \right] - 1 \right\}, \end{aligned} \quad (9)$$

where $T(r)$ is the plasma temperature as a function of the distance r from the star's center. This expression is consistent with the one given in Refs. [35, 50, 52–59]. Since nuclei are assumed to be at rest, energy conservation tells that the incoming photon and the outgoing ALP have the same energy, i.e. $E_a = \sqrt{p^2 + m_a^2} = \sqrt{k^2 + \omega_{\text{pl}}^2}$, and thus, momenta k and p can be seen as functions of the axion energy E_a .

B. Photon Coalescence

Axions could also be produced in the stellar plasma via photon coalescence $\gamma(\mathbf{k}_1) + \gamma(\mathbf{k}_2) \rightarrow a(\mathbf{p}_a)$ in which two photons annihilate into an axion (see Fig. 1 right panel).

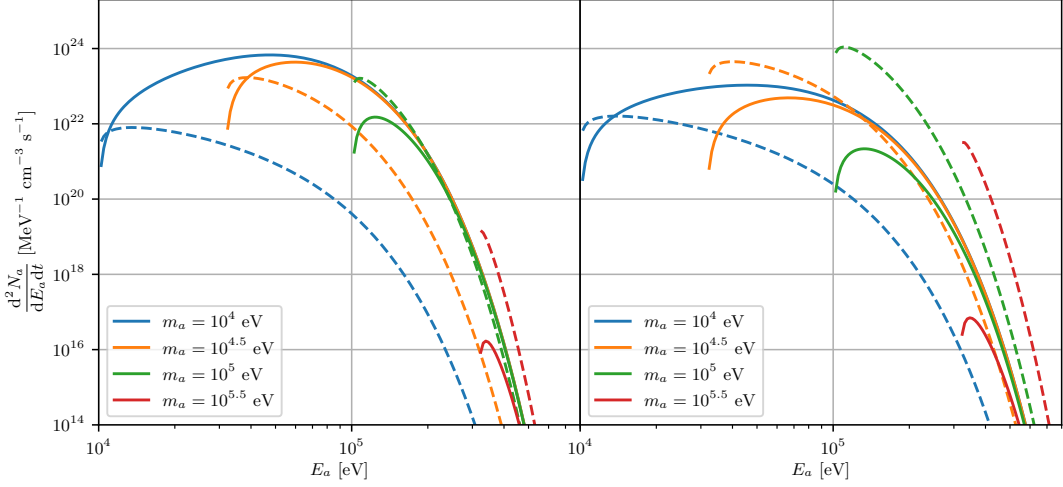


Figure 2: Production spectra for the Primakoff process (solid lines) and photon coalescence (dotted lines) for four choices of axion mass: $m_a = 10^4$ eV (blue), $10^{4.5}$ eV (orange), 10^5 eV (green), and $10^{5.5}$ eV (orange). In the left panel, we set the values of plasma frequency, temperature, and the inverse Debye length as $\omega_{\text{pl}} = 3$ keV, $T = 15$ keV, and $\kappa = 50$ keV which reproduce the environment of the core of a sample HR star (see Fig. 7 for details). The right panel assumes WR star-like environment with $\omega_{\text{pl}} = 3$ keV, $T = 20$ keV, and $\kappa = 5$ keV.

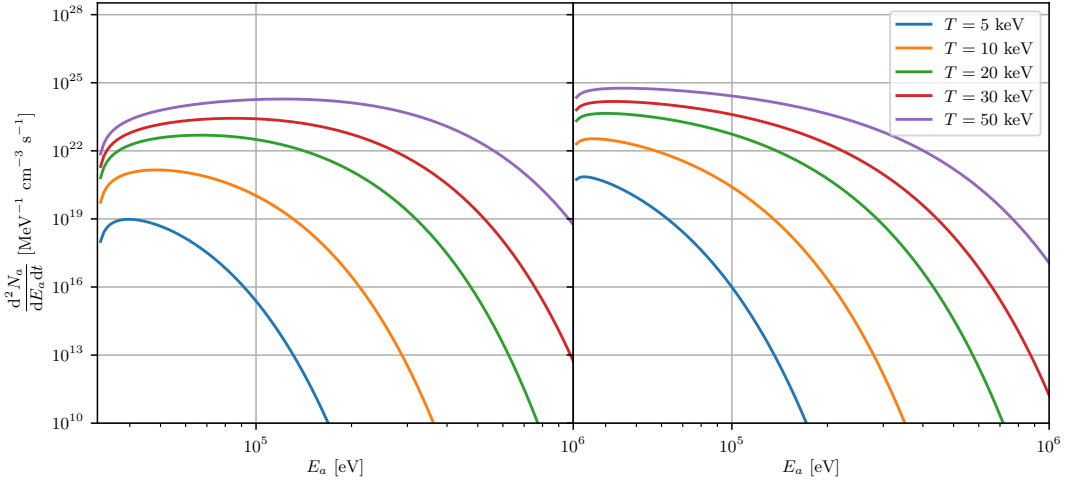


Figure 3: The plot comparing the production spectra of axions in the plasma with different temperatures $T = 5$ keV (blue), 10 keV (orange), 20 keV (green), 30 keV (red), and 50 keV (purple). The axion mass, the plasma frequency, and the axion-photon coupling are fixed to $m_a = 10^{4.5}$ eV, $\omega_{\text{pl}} = 3$ keV, and $g_{a\gamma} = 10^{-6}$ GeV $^{-1}$, respectively, i.e. the production rate is calculated at the core of HB star. The left (right) panel shows the production rate of the Primakoff process (photon coalescence).

Its production rate is given by

$$\begin{aligned} \frac{dn_a}{dt}(r, t) = & \sum \int \frac{d^3 \mathbf{k}_1}{(2\pi)^3 2E_1} f_1(E_1) \int \frac{d^3 \mathbf{k}_2}{(2\pi)^3 2E_2} f_2(E_2) \\ & \times \int \frac{d^3 \mathbf{p}_a}{(2\pi)^3 2E_a} (2\pi)^4 \delta^{(4)}(k_1 + k_2 - p_a) \frac{1}{S} |\mathcal{M}|^2, \end{aligned} \quad (10)$$

where $k_1^\mu = (E_1, \mathbf{k}_1)$, $k_2^\mu = (E_2, \mathbf{k}_2)$, and $p_a^\mu = (E_a, \mathbf{p}_a)$ are four-momenta of the incoming photons (denoted by 1 and 2 for convenience) and the outgoing axion. The

symmetry factor is $S = 2$ for photon coalescence. The summation runs over the spin and polarization states of the photons. The invariant matrix element of this process is given by

$$\mathcal{M} = -ig_{a\gamma} \epsilon^\mu(k_1) \epsilon^\nu(k_2) k_1^\rho k_2^\sigma \epsilon_{\mu\nu\rho\sigma}. \quad (11)$$

For simplicity, we approximate $s = (k_1 + k_2)^2 \approx m_a^2$ where s is one of the Mandelstam variables. Then, the spin- and polarization-summed squared invariant matrix is reduced to $|\mathcal{M}|^2 = g_{a\gamma}^2 m_a^2 (m_a^2 - 4\omega_{\text{pl}}^2) / 2$. Taking a

derivative with respect to E_a and performing integrations again gives the production spectrum:

$$\frac{d^2 n_a}{dE_a dt}(r, t, E_a) = \frac{g_{a\gamma}^2 m_a^2}{128\pi^3} (m_a^2 - 4\omega_{\text{pl}}^2) \frac{T}{e^{E_a/T} - 1} \times \ln \left[\frac{(1 - e^{E_{\text{max}}/T})(e^{E_a/T} - e^{E_{\text{min}}/T})}{(1 - e^{E_{\text{min}}/T})(e^{E_a/T} - e^{E_{\text{max}}/T})} \right], \quad (12)$$

where E_{max} (E_{min}) is the maximum (minimum) energy of each photon that can produce an axion with mass m_a :

$$E_{\text{min,max}} = \frac{1}{2} \left(E_a \mp \sqrt{E_a^2 - m_a^2} \sqrt{1 - \frac{4\omega_{\text{pl}}^2}{m_a^2}} \right). \quad (13)$$

This expression coincides with the result in Ref. [42] in the limit of low temperature compared to the axion mass: $T \ll m_a$.

Fig. 2 compares the axion production spectra for the Primakoff process (solid lines) and photon coalescence (dashed lines). The left panel assumes the core of HB stars and the right panel assumes that of WR stars. The production spectra are calculated for four benchmark values of axion mass: $m_a = 10^4$ eV (blue), $10^{4.5}$ eV (orange), 10^5 eV (green), and $10^{5.5}$ eV (orange). The production spectra are suppressed in the limits of $E_a \rightarrow m_a$ due to kinematics and $E_a \gg 3T$ due to Boltzmann suppression. As noted previously, the light axions are produced more efficiently by the Primakoff process while heavier axions are more efficiently produced by photon coalescence. This tendency is more pronounced in a WR star-like environment (right panel). Fig. 3 exhibits the axion production spectra for the Primakoff process (left panel) and photon coalescence (right panel) for different plasma temperatures: $T = 5$ keV (blue), 10 keV (orange), 20 keV (green), 30 keV (red), and 50 keV (purple). As expected, more axions are produced in the plasma with higher temperatures.

C. Thermal Corrections

In practice, photons acquire a longitudinal mode in plasma [60–66], in addition to the two transverse modes. Let us denote the four-momentum vector of a photon and an electron/positron in the rest frame of the plasma by $K^\mu \equiv (\omega, \mathbf{k})$ and $P \equiv (E, \mathbf{p})$, respectively. The longitudinal mode is described as the mode with the polarization vector whose spatial part is parallel to the wave vector; $\epsilon_L^\mu = (k^2, \omega \mathbf{k})/k\sqrt{K^2}$. One of other three degrees of the photon's polarization vector is taken up by the condition $K^\mu \epsilon_\mu = 0$, which guarantees the polarization tensor of photons $\Pi_{\mu\nu}$ to be transverse; $K^\mu \Pi_{\mu\nu} = K^\nu \Pi_{\mu\nu} = 0$. The remaining two degrees of freedom describe transverse modes, i.e. polarization tensors of transverse modes are chosen to be orthogonal to both K^μ and ϵ_L .

The effect of the finite-temperature plasma is incorporated by calculating the polarization tensor of photons, including the interaction of photons with surrounding electrons and positrons. Summing over all 1-particle irreducible diagrams, one finds the full propagator $\Delta_{\mu\nu}$ where $\Pi_T(\omega, \mathbf{k})$ and $\Pi_L(\omega, \mathbf{k})$ characterize its poles, corresponding to two modes of wave propagation in the plasma. In the Coulomb gauge ($\nabla \cdot \mathbf{A} = 0$), the photon propagator reads as [67]

$$\begin{aligned} \Delta_{00} &= \frac{1}{K^2 - \Pi_L} \frac{K^2}{|\mathbf{k}|^2}, \\ \Delta_{0i} &= 0, \\ \Delta_{ij} &= \frac{P_{\mu\nu}}{K^2 - \Pi_T}. \end{aligned} \quad (14)$$

Π_T and Π_L can be obtained analytically only when $T \gg |\mathbf{k}|, \omega$, and its real part has to do with the dispersion relation while its imaginary part governs the damping behavior of the photon wave. The plasma of stars considered in this paper is nonrelativistic ($T \ll m_e$) and nondegenerate ($m_e - \mu \gg T$). Up to the $\mathcal{O}(T/m_e)$ term, one finds

$$\text{Re}\Pi_T(\omega, \mathbf{k}) = \omega_p^2 \left(1 + \frac{|\mathbf{k}_T|^2}{\omega_T^2} \frac{T}{m_e} \right), \quad (15)$$

$$\text{Re}\Pi_L(\omega, \mathbf{k}) = \omega_p^2 \frac{K_L^2}{\omega_L^2} \left(1 + 3 \frac{|\mathbf{k}_L|^2}{\omega_L^2} \frac{T}{m_e} \right). \quad (16)$$

At the one-loop level, the contributions from ions to the photon self-energy can be approximately included just by summing over all ions; $\Pi = \sum_{i=e,\text{ions}} \Pi_i$ because photons do not address the internal structure [64]. The real parts remain approximately the same because $m_e \ll m_{\text{ions}}$. The location of the pole of the propagator determines the dispersion relation of each mode:

$$\omega_T^2 = |\mathbf{k}_T|^2 + \text{Re}\Pi_T(\omega, \mathbf{k}), \quad (17)$$

$$\omega_L^2 = \frac{\omega_L^2}{K_L^2} \text{Re}\Pi_L(\omega, \mathbf{k}). \quad (18)$$

Insertions of thermal photon diagrams can be interpreted as the modification of the photon self-energy, and thus, the renormalization of the photon field is required. In the finite temperature plasma, the wave function of the photon field associated with the different frequencies is modified differently in a temperature-dependent way. As a function of the frequency and the temperature of the plasma, the wave-function renormalization constant is given by

$$Z_T = \left[1 - \frac{\partial \Pi_T}{\partial \omega_T^2} \right]^{-1} = 1 - \frac{\omega_p^2 |\mathbf{k}_T|^2}{\omega_T^4} \frac{T}{m_e}, \quad (19)$$

$$\begin{aligned} Z_L &= \frac{|\mathbf{k}_L|^2}{\omega_L^2} \left[-\frac{\partial (|\mathbf{k}_L|^2 \Pi_L / K_L^2)}{\partial \omega_L^2} \right]^{-1} \\ &= \frac{\omega_L^2}{\omega_p^2} \left(1 - 6 \frac{|\mathbf{k}_L|^2}{\omega_L^2} \frac{T}{m_e} \right), \end{aligned} \quad (20)$$

again up to the order of T/m_e .

We checked that (i) the thermal correction is negligible in our case mainly because of the small plasma temperature compared to the electron mass: $T/m_e \ll 1$, (ii) in photon coalescence, the annihilation of the transverse mode photons gives the dominant contribution to axion production, and the effect of the longitudinal mode photons can be safely neglected. Therefore, we neglect the thermal corrections in the following and calculate the axion production rates by using Eqs. (9) and (12).

III. FLUENCE OF PHOTONS OBSERVED AT THE EARTH

In this section, we assess the detectability of photon signals arising from the decay of keV-MeV axions produced inside massive stars. In concrete terms, we (i) construct the stellar models by using the stellar evolution code MESA [68–72], (ii) compute the production rate of axions inside stars, (iii) estimate the fraction of axions that escape from the stellar plasma without undergoing spontaneous decay, (iv) calculate the flux of X -ray/ γ -ray, produced by the decay of axions, at the detector on or near Earth, and (v) examine its observability by current/future telescopes. Sec. III A begins with a brief summary of the stellar evolution, followed by a discussion of our choice of target stars as axion laboratories and the methodology for modeling those stars using the MESA stellar evolution code. Estimations of the fraction of axions undergoing spontaneous decay outside stars and subsequent X -ray/ γ signal at the detector are provided in Sec. III B. Sec. III C provides information on telescopes and discusses the potential astrophysical backgrounds.

A. Stellar models

1. History of stellar evolution

Formation of protostars takes place in the dense region of the molecular cloud in the interstellar medium. This dense region experiences gravitational contraction, leading to an increase in temperature and pressure. Hydrogen is ignited once the temperature is reached high enough, and consequently, the gravitational contraction force is balanced by the outward pressure from nuclear fusion. These hydrogen-burning stars occupy the main sequence in the Hertzsprung–Russell diagram. MS stars primarily consist of hydrogen at the point of their formation. They generate energy by burning hydrogen in the core either via the pp-chain reaction in less massive MS stars or CNO-cycle in massive MS stars. These processes heat MS stars up to $\mathcal{O}(\text{keV})$ at the core.

MS stars become red-giant branch (RGB) stars when they use up hydrogen fuel in the core. This transition takes place $\mathcal{O}(10^{8-10})$ yrs) after low- or intermediate-mass stars are born. The core of RGB stars is mainly

made of ${}^4\text{He}$, which is a product of the pp-chain and the CNO-cycle. Their cores are inert, and as a result, they contract and are heated. A surrounding shell of hydrogen continues to undergo fusion, leading to the expansion of RGB stars to $\mathcal{O}(100R_\odot)$.

In case of low-mass stars ($M_{\text{init}} \lesssim 2M_\odot$), degeneracy pressure of a helium core ends up dominating over thermal pressure, i.e. a helium core becomes degenerate. A core keeps contracting by releasing its gravitational potential energy, increasing a core temperature until helium is ignited. Ignition of helium leads to the helium flash, a release of enormous energy in a very short time. High-mass stars ($M_{\text{init}} \gtrsim 2M_\odot$) undergo instead a gradual emission of energy since its high core temperature prevents a degenerate helium core, leading to a less intense dynamics. Stars burning helium in their core are called HB stars whose temperature and radius are typically $\mathcal{O}(10)$ keV and $\sim 20R_\odot$, respectively. Fig. 4 illustrates the composition of a HB star at the end of the HB phase.

Helium burning yields ${}^{12}\text{C}$, which subsequently produces ${}^{16}\text{O}$. Those reactions cease once helium in the core is depleted. Following this, the core made of carbon and oxygen starts contracting while hydrogen and helium shells are expanded to $\mathcal{O}(100)R_\odot$. These stars, asymptotic giant branch (AGB) stars, are then evolved to white dwarfs, neutron stars, or black holes depending on their initial mass.

Initially superheavy stars ($M_{\text{init}} \gtrsim 30M_\odot$) could follow a different evolutionary history and become a rarer class of stars called Wolf-Rayet stars [73]. WR stars are hot and luminous stars whose hydrogen envelopes are stripped away due to either a wind or a binary interaction. They are categorized into the nitrogen-sequence (WN), the carbon-sequence (WC), and the oxygen-sequence (WO) WR stars by their He, N, C, and O emission lines. The categorization by its surface abundance of nuclei is still not fully established. For simplicity, we assume that WR stars are classified by the surface abundances of relevant nuclei. A WR star enters the WN phase when its surface abundance of hydrogen is reduced to 5%, the WC phase when its surface abundance of carbon reaches 2%, and the WO phase when its surface abundance of oxygen becomes 2% as assumed in Ref. [44]. Fig. 5 illustrates the composition of WR stars. The right panel plots the mass abundance of each nucleus as a function of the distance from the center of a WR star just entering the WC phase.

2. Target stars as axion laboratories

In this paper, we focus on stars beyond the MS, namely, the HB stars and WR stars, as production sites of axions because they have several appealing features: (i) high temperature of the plasma, $T_{\text{HB}} \sim 10$ keV, is about an order higher than that of MS stars, leading to more efficient production of axions, and (ii) small radius of their

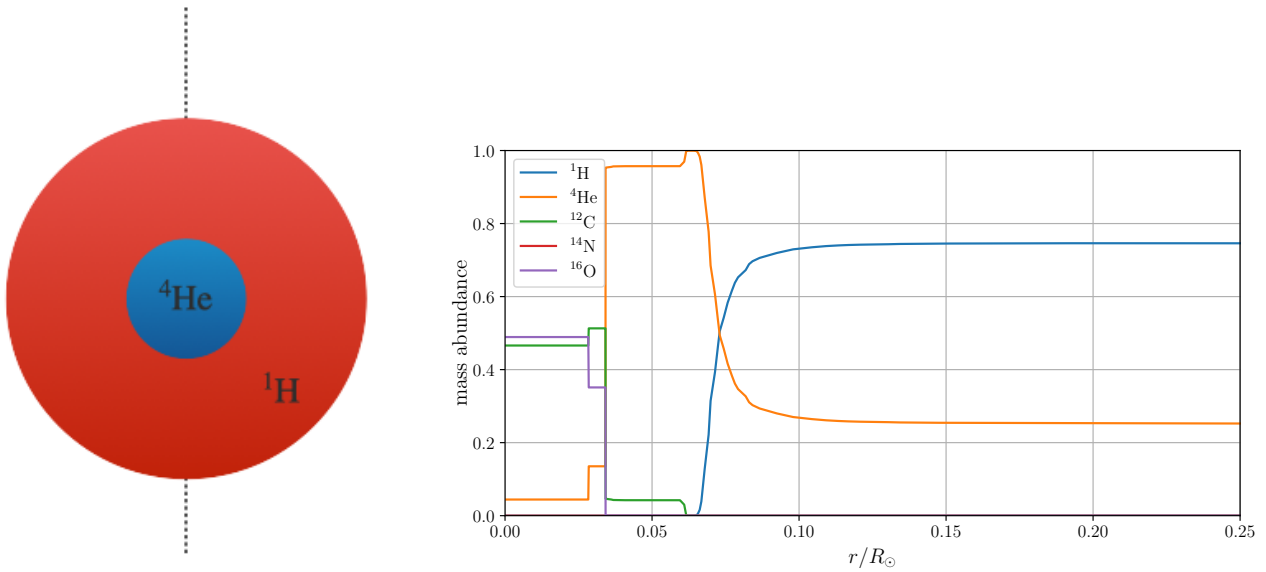


Figure 4: Left: The schematic diagram of a HB star. It consists of a helium core and hydrogen shell at the onset of the horizontal branch phase. Heavier nuclei such as ^{12}C and ^{16}O are produced via helium burning subsequently. Right: The mass abundance of each nucleus as a function of the distance from the center of the star at the moment when the helium abundance at the center drops to 5%. The initial mass, initial helium abundance, and initial metallicity are chosen as $(M_{\text{init}}, Y, Z) = (0.83M_{\odot}, 0.254, 0.0005)$.

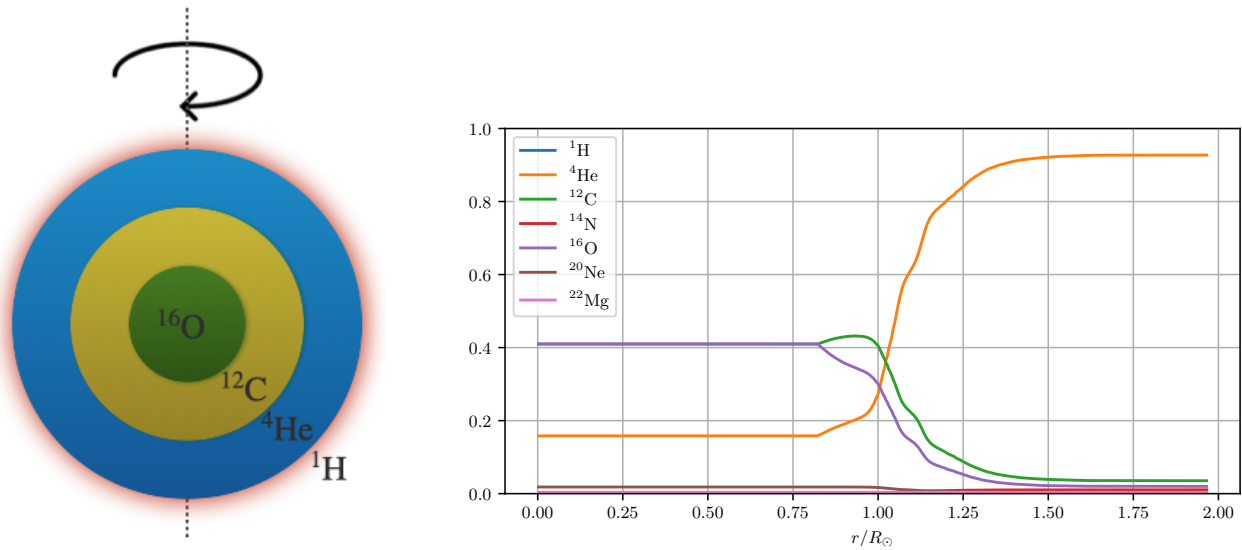


Figure 5: Left: The schematic diagram of a WR star. The WR star consists of helium 4 and heavier nuclei (e.g. ^{12}C , ^{16}O). The hydrogen envelope is almost stripped away due to its fast rotation. Right: The mass abundance of each nucleus as a function of the distance from the center of the star at the onset of the WC phase. The initial mass, initial rotational velocity, and initial metallicity are chosen as $(M_{\text{init}}, v_{\text{rot}}, Z) = (90M_{\odot}, 180 \text{ km/s}, 0.018)$.

photosphere, roughly an order of magnitude smaller than that of RGB stars and AGB stars, resulting in less absorption of photons signal induced by spontaneous decay of axions. In the following, we briefly outline the astrophysical objects considered in this study and describe our approach to modeling them by using the MESA stellar evolution code.

a. HB stars Globular clusters consist of millions of gravitationally bounded stars with roughly the same age and chemical composition. Thus, globular clusters in the right age could host a large number of HB stars. One of the largest Galactic globular clusters is NGC 2808 ($M = 1.42 \times 10^6 M_{\odot}$), which is located at $d = 31.3$ kly away from us. NGC 6397 ($M = 1.15 \times 10^5 M_{\odot}$), though about an order of magnitude lighter than NGC 2808, is another

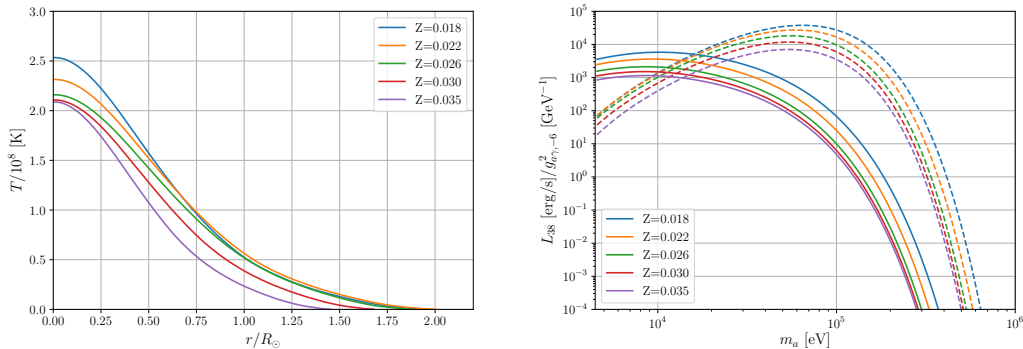


Figure 6: Left: The temperature profile of a WR star at the onset of the WC phase as a function of its radius. Five different metallicity values $Z = 0.018, 0.022, 0.026, 0.030,$ and 0.035 are considered. We set an initial mass and a rotational velocity at the zero-age MS as $85M_{\odot}$ and $v = 150$ km/s. Right: Luminosity of axions produced in a WR star with different metallicity by the Primakoff process (solid lines) and photon coalescence (dotted lines). The luminosity is normalized by dividing it by the axion-photon coupling strength $g_{a\gamma} = 10^{-6}$ GeV^{-1} .

	NGC 2808	NGC 6397
Mass (M_{\odot})	1.42×10^6	1.15×10^5
Radius (ly)	62.8	17.2
Distance (kly)	31.3	7.5
Right ascension	09 ^h 12 ^m 03	17 ^h 40 ^m 42
Declination	-64°51'48"	-53°40'27"
N_{HB}	1200	105

Table I: Properties of the two globular clusters used in this study. Data of the radius, distance, and right ascension are taken from Refs. [74–76]. Masses and the number of HB stars are estimated in Refs. [77] and [78, 79], respectively.

promising object because of its vicinity to the Earth with $d = 7.5$ kly. Photometry estimates the number of HB stars in each globular cluster as $N_{\text{HB}} \sim 1200$ for NGC 2808 and $N_{\text{HB}} \sim 105$ for NGC 6397, respectively [78, 79]. Properties and locations of these globular clusters are summarized in Table I.

The stellar models are constructed using an open-source 1D stellar evolution code MESA [68–72] version r22.11.1. A model of a HB star is evolved from the pre-MS to the terminal-age core helium burning phase. The initial mass, the helium abundance, and the metallicity of a sample star are set as $M_{\text{init}} = 0.83M_{\odot}$, $Y = 0.254$, and $Z = 0.0005$. For simplicity, we assume that a sample star represents the average property of HB stars in globular clusters. Accordingly, we approximate that the total production rate of axions in each globular cluster as the production rate of a sample star multiplied by N_{HB} .

b. WR stars For WR stars, we focus on the Quintuplet cluster. The Quintuplet cluster is one of the most massive young clusters in the Milky Way near the Galactic Center. The spectroscopic survey shows that this cluster contains 71 massive stars among which 13 are in the WC and 1 is in the WN phase. Their ages are

estimated to fall within the range $t \in (3.0, 3.6)$ Myr [80]. Requiring the observed nitrogen abundance of WNh stars in the Arches cluster matches with that estimated by MESA and assuming the Arches cluster and the Quintuplet cluster have the same metallicity, the metallicity of the Quintuplet cluster is estimated to be in the range $Z \in (0.018, 0.035)$. For a given metallicity Z , the helium abundance Y is found by the following formula:

$$Y = Y_p + \left(\frac{Y_{\text{protosolar}} - Y_p}{Z_{\text{protosolar}}} \right) Z, \quad (21)$$

where $Y_p = 0.248$ is the primordial helium abundance estimated from a combination of measurements of the CMB power spectra, lensing, and baryon acoustic oscillation [81], $Y_{\text{protosolar}} = 0.2703$ is the protosolar helium abundance, and $Z_{\text{protosolar}} = 0.0134$ is the protosolar metallicity [82]. Each star in the Quintuplet cluster is evolved from the pre-MS until near a core-collapse by using MESA.

Fig. 6 plots the temperature profile (left) and luminosity of axions as a function of the axion mass (right) for a sample WR star with different metallicity values. The higher initial metallicity leads to a more efficient mass loss of stars, resulting in larger luminosity of axions [44]. On the other hand, stars with lower initial metallicity tend to predict a smaller radius at the beginning of the WC phase that allows more axions to escape from their photospheres. Since the photon signal from axion decay has nontrivial dependence on the initial metallicity Z , we made stellar models and estimated the detectability of photons both for high ($Z = 0.035$) and low ($Z = 0.018$) metallicities.

Since the Quintuplet cluster is located near the Galactic center, the distance to the cluster is approximated by the Galactocentric distance of the sun $d_{\text{GC}} \sim 8$ kpc [83]. Simulations by MESA revealed that WR stars in the WC phase have a higher temperature and a smaller radius,

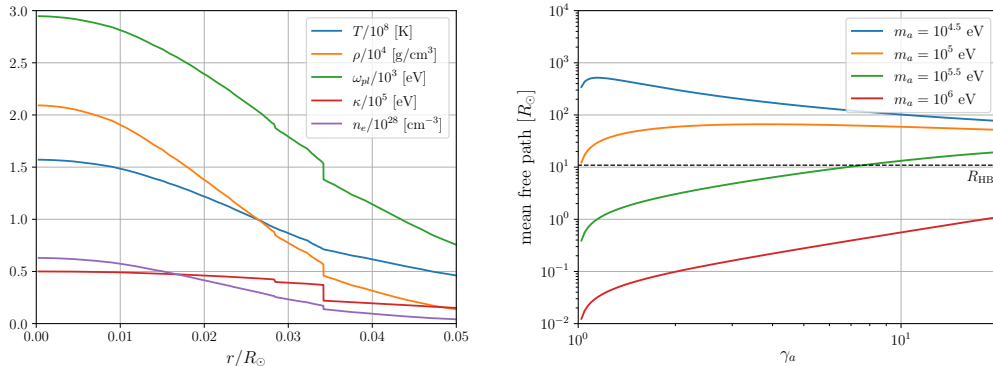


Figure 7: Left: The profiles of temperature (blue), energy density (orange), plasma frequency (green), the screening scale κ (red), and number density of electrons (purple) as a function of the distance from the stellar center. This snapshot is taken when central mass abundance of helium 4 reaches $X_{\text{He}} = 0.6$. The most internal $0.05R_{\odot}$ or $0.44M_{\odot}$ regions are plotted. Right: The mean free path of an axion with a mass, $m_a = 10^{4.5}, 10^5, 10^{5.5}$, and 10^6 eV, with the Lorentz factor $\gamma_a \in [1, 20]$ is shown. The mean free path is evaluated with the temperature at the HB star core. The dashed black line represents the radius of a sample HB star $R_{\text{HB}} = 10.9R_{\odot}$.

implying that they dominantly contribute to the photon signal from axion decay. Therefore, we consider the production of axions only in 13 WC stars.

The sample of 13 WC stars is calculated in the following way. We first randomly chose an initial mass M_{init} and a rotational speed v_{rot} of a sample star. Those are assumed to follow the Kroupa initial mass function [84] and the Gaussian distribution function with a mean velocity $\mu_{\text{rot}} = 100$ km/s and a velocity dispersion $\sigma_{\text{rot}} = 140$ km/s [85, 86]. The initial mass is assumed to fall within the range $M_{\text{init}} \in (20, 200)M_{\odot}$. This stellar model is evolved from its pre-MS phase until it enters the WC phase. Repeating this process, we construct $\mathcal{O}(100)$ samples of WC stars. Among these samples, only those that predict the age of a star consistent with the spectral analysis, i.e. in the range of (3.0, 3.6) Myr at the onset of the WC phase, are retained in our analysis and the rest are discarded. A detailed description of the choice of parameters in our code can be found in Appendix A.

The left panel of Figs. 7 and 8 show the plasma temperature, density, plasma frequency, and Debye screening length of a sample HB star and WR star as a function of the distance from the stellar center, respectively. The mean free path of axions with several benchmark masses is plotted in the right panels.

B. Photon signal at the Earth

Integrating the axion production spectra given in Eqs. (5) and (10) over the volume of the star, we arrive at the total axion production rate, i.e. the number of axions produced with energy E per unit time:

$$\frac{d^2 N_a}{dE dt}(t, E) = \int_0^{R_s} dr 4\pi r^2 \frac{d^2 n_a}{dt dE}(r, t, E). \quad (22)$$

where R_s is the stellar radius.

An axion could undergo the reconversion into a photon in presence of a magnetic field or spontaneously decay into two photons inside a star. These photons are subsequently absorbed in the plasma and therefore do not contribute to an observable signal. In order to incorporate this effect, we rewrite Eq. (22) as

$$\frac{d^2 N_a}{dE dt}(E) = \int_0^{R_s} dr 4\pi r^2 \frac{d^2 n_a}{dt dE}(r, E) e^{-\tau(d, E)}, \quad (23)$$

where τ is the optical depth of axions:

$$\tau(r, \phi, E) = \int_0^d dl \lambda^{-1}(l, E), \quad (24)$$

λ is the overall mean free path of axions, and d is the distance that an axion travels before escaping from the star's photosphere.

The overall mean free path can be expressed in terms of the mean free path of each process: $\lambda^{-1} = \lambda_{\text{Primakoff}}^{-1} + \lambda_{\text{Coalescence}}^{-1}$. Each mean free path is obtained by

$$\lambda_i = \beta_a \Gamma_i^{-1} = \frac{\beta_a^2 E^2}{2\pi^2 e^{E/T}} \left(\frac{d^2 N_a}{dE dt} \Big|_i \right)^{-1}. \quad (25)$$

Here $\beta_a = \sqrt{1 - (m_a/E)^2}$ is the axion speed. The right panels of Figures 7 and 8 show the overall mean free path for several choices of the axion mass. These plots imply that heavy axions have shorter mean free paths. For comparison, we also show by horizontal dashed lines the typical size of the star; only the axions with a mean free path larger than this value can escape the star.

Once the axions escape the photosphere of the star and decay into photons, a fraction of them might be detected on the Earth. Fig. 9 illustrates the geometry of detection

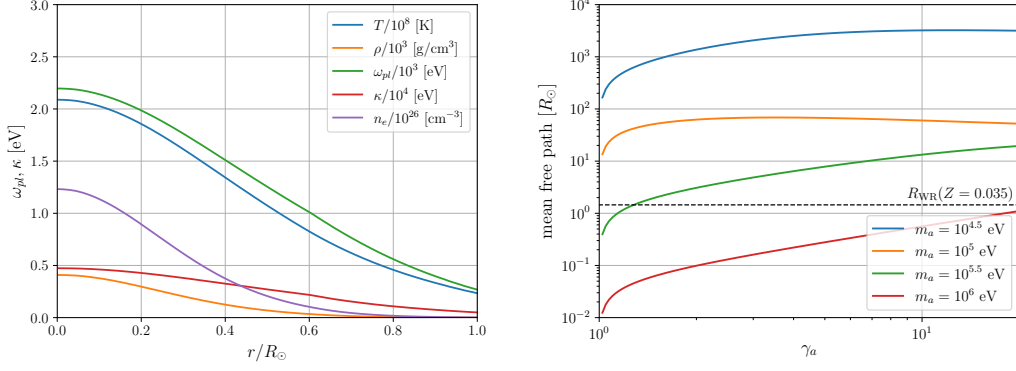


Figure 8: Left: The profiles of temperature (blue), energy density (orange), plasma frequency (green), the screening scale κ (red), and number density of electrons (purple) of a WR star with $Z = 0.035$ and an initial mass $85M_{\odot}$ when it reaches the WC phase. The most internal R_{\odot} region is plotted. Right: The mean free path of an axion with several masses with the Lorentz factor $\gamma_a \in [1, 20]$ at the WR star core. The dashed black line represents the radius of a sample WR star, $R_{\text{WR}} = 1.45R_{\odot}$, for a metallicity $Z = 0.035$.

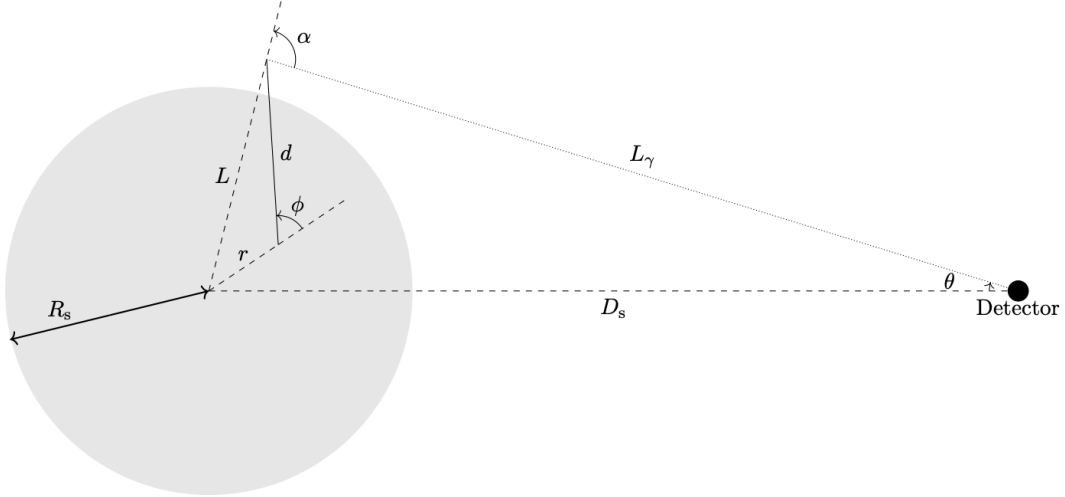


Figure 9: An illustration of the photon detection from spontaneous decay of axions produced inside a star. Axions are produced in the stellar plasma either by the Primakoff process or photon coalescence. Axions that decay outside the photosphere could yield an observable photon signal at the Earth. The radius of the photosphere is denoted by R_s and the distance to the star is D_s .

of photons from the decay of axions produced in the star (see e.g. Refs. [46, 87] for a detailed discussion of the geometry effect). The distance L the axion travels before decaying can be expressed as a function of the radius of the photosphere R_s , the radial distance r of the point where an axion is produced, and the inclination angle ϕ of the axion momentum vector relative to the radial direction:

$$L = -r \cos \phi + \sqrt{R_s^2 - r^2 \sin^2 \phi}. \quad (26)$$

The differential of the fluence F_{γ} of photons, i.e., the number of photons per unit time per unit area, from ax-

ion decay is given by [34, 35, 88]

$$dF_{\gamma} = 2 \cdot \text{BR}_{a \rightarrow \gamma\gamma} \cdot \frac{1}{4\pi D_s^2} \cdot \frac{d^2 N_a}{dE dt} dE \cdot f_{c_{\alpha}}(E, c_{\alpha}) dc_{\alpha} \\ \times \frac{\exp[-L/l_a(E)]}{l_a(E)} dL \cdot \Theta_{\text{cons.}}(E, c_{\alpha}, L), \quad (27)$$

where the different factors are explained as follows: (i) The factor 2 takes into account the number of photons produced in each decay of an axion. (ii) $\text{BR}_{a \rightarrow \gamma\gamma}$ is the branching ratio of the decay of an axion into two photons. Since we neglect all couplings except the axion-photon

coupling, this branching ratio is set as 1. (iii) $\frac{1}{4\pi D_s^2}$ is a geometric factor for the decrease in luminosity, assuming an isotropic production of axions. (iv) $\frac{d^2 N_a}{dE dt} dE$ is the number of axions that escape from the stellar photosphere per unit time. (v) $f_{c_\alpha}(E, c_\alpha)$ is the distribution of the angle α :

$$f_{c_\alpha}(E, c_\alpha) = \frac{m_a^2}{2E^2(1 - c_\alpha \beta_a)^2}, \quad (28)$$

as a function of the axion mass, energy and velocity. Here $c_\alpha \equiv \cos \alpha$. (vi) $\frac{\exp[-L/l_a(E)]}{l_a(E)} dL$ is the probability for an axion to decay within a distance $[L, L + dL]$ from the source. The decay length of an axion l_a is given by

$$l_a(E) = \frac{\beta_a \gamma_a}{\Gamma_0^{a \rightarrow \gamma \gamma}}, \quad (29)$$

where $\Gamma_0^{a \rightarrow \gamma \gamma} = g_{a\gamma}^2 m_a^3 / 64\pi$ is the spontaneous decay rate of an axion in the rest frame. (vii) $\Theta_{\text{cons.}}(E, c_\alpha, L)$ is the constraint placed on the energy of an axion E , the angle α , and the distance L so that one of the photons from the decay of an axion arrives at the detector on the Earth. This constraint is given by a product of the Heaviside functions:

$$\begin{aligned} \Theta_{\text{cons.}}(E, c_\alpha, L) = & \Theta(E_{\text{max}} - \omega_\gamma(\omega, c_\alpha)) \\ & \times \Theta(\omega_\gamma(\omega, c_\alpha) - E_{\text{min}}) \\ & \times \Theta(c_\theta(c_\alpha, L)) \\ & \times \Theta(c_\theta(c_\alpha, L) - c_\alpha) \\ & \times \Theta(L - R_s), \end{aligned} \quad (30)$$

where ω_γ is the energy of the photon observed at the Earth, $c_\theta = \cos \theta$, and L_γ is the distance that a photon has to travel until it arrives at the detector. These are given by

$$\omega_\gamma(E, c_\alpha) = \frac{m_a^2}{2E(1 - c_\alpha \beta_a)}, \quad (31)$$

$$c_\theta(c_\alpha, L) = \frac{L_\gamma^2 + D_s^2 - L^2}{2L_\gamma D_s}, \quad (32)$$

$$L_\gamma = L \left(\sqrt{\frac{D_s^2}{L^2} - 1 + c_\alpha^2} - c_\alpha \right). \quad (33)$$

Each constraint in Eq. (30) is described below:

- $\Theta(E_{\text{max}} - \omega_\gamma(\omega, c_\alpha)) \Theta(\omega_\gamma(\omega, c_\alpha) - E_{\text{min}})$: The energy of a photon is in the range of each energy band $[E_{\text{min}}, E_{\text{max}}]$ of the detector.
- $\Theta(c_\theta(c_\alpha, L))$: The photon reaches the detector without being shielded by the Earth.
- $\Theta(c_\theta(c_\alpha, L) - c_\alpha)$: The parameters geometrically allow a photon to arrive at the detector.

- $\Theta(L - R_s)$: The axion decays beyond the photosphere with a radius R_s .

The differential fluence in Eq. (27) is integrated over energy and angle α subject to the constraints given above to obtain the total fluence of the photon signal induced by axion decay, which is then compared with the experimental sensitivity for a given telescope to derive the ALP sensitivity curves in the next section.

C. Telescopes

The energy of axions produced in HB and WR stars is comparable either to the temperature of their plasma (for $T \gtrsim m_a$) or the rest mass of axions (for $T \lesssim m_a$). Those axions then spontaneously decay into two photons. As shown in Fig. 6 right panel, the spectrum of photons is expected to have a peak at $E_\gamma \sim \mathcal{O}(10 - 100)$ keV, and thus, a hard X-ray telescope or MeV gamma-ray telescope is best suited for observing those photons.

We estimated the observability of photons by several existing hard X-ray telescope missions XMM-Newton [89], NuSTAR [90] and INTEGRAL (which includes IBIS/ISGRI [91], IBIS/PICsIT [92], SPI [93], and JEM-X [94]), SWIFT [95], eROSITA [96], Insight-HXMT/HE [97], and one future X-ray mission COSI [98], as well as several future soft gamma-ray telescope missions AMEGO/AMEGO-X [99, 100], ASTROGAM/e-ASTROGAM [102, 105]), GECCO [104] and APT [101]. The sensitivity range of each telescope is summarized in Table II. In general, the angular resolution of telescopes depends on the energy of incoming photons. Moreover, a telescope could be operated in more than one mode each of which has a different angular resolution; for example, the angular resolution of GECCO is $\sim 1'$ in the Mask mode while it is $4^\circ - 8^\circ$ in the Compton mode. For simplicity, we assume the angular resolution is independent of the energy of injected photons and is the value listed in Table II. In order to estimate the detectability of photons, we used the 3σ continuum sensitivity of the telescopes [106] by assuming the observation times summarized in the Table. We found that INTEGRAL SPI gives the best sensitivity in the relevant ALP parameter space of our interest. This is mainly because of its energy sensitivity range which covers the peak ALP emission spectrum from HB stars and WR stars, as well as its large angular resolution which ensures more photon collection per pixel from the ALP decay region.

IV. DETECTABILITY OF PHOTON SIGNALS

In this section, we present our results on the detection of photons resulting from the spontaneous decay of axions produced inside HB and WR stars. Fig. 10 highlights the regions in the $m_a - g_{a\gamma}$ parameter space that can be probed by INTEGRAL SPI. We compare our result to

Mission	Sensitivity Range	Angular Resolution (at Energy)	Mission Status	Effective Area	Observation Time
XMM-Newton [89]	0.1-15 keV	12'' (2-10 keV)	1999-present	~3000 cm ²	10 ⁴ s
NuSTAR [90]	5 keV - 80 keV	18''	2012-present	~1000 cm ²	10 ⁶ s
INTEGRAL IBIS/ISGRI [91]	15 keV - 1 MeV	12''	2002-2023	250 cm ²	10 ⁵ s
INTEGRAL IBIS/PICsIT [92]	170 keV - 10 MeV	12'	2002-2023	~1400 cm ²	10 ⁵ s
INTEGRAL SPI [93]	20 keV - 8 MeV	2.5°	2002-2023	~3000 cm ²	10 ⁶ s
INTEGRAL JEM-X [94]	3 keV - 35 keV	3'	2002-2023	400 cm ²	10 ⁶ s
SWIFT (BAT) [95]	15-150 keV	22'	2004-present	5200 cm ² (15 keV)	0.7×19 yrs
eROSITA [96]	0.2-10 keV	35'' (2-8 keV)	2019-present	1500 cm ²	10 ⁵ s
Insight-HXMT/HE [97]	20 keV - 250 keV	6'	2017-present	4096 cm ²	~10 ⁵ s
COSI [98]	200 keV - 5 MeV	~4° (1 MeV)	2027 (planned)	~300 cm ²	2 yrs
AMEGO (Compton) [99]	200 keV - 10 MeV	~4° (1 MeV)	Concept	~300 cm ²	0.24×5 yrs
AMEGO-X [100]	100 keV - 1 GeV	~10°	Concept	3500 cm ²	3 yrs
APT (Compton) [101]	200 keV - 10 MeV	~5° (1 MeV)	Concept	10,000 cm ²	0.82×5 yrs
ASTROGAM [102]	100 keV - 1 GeV	~1.5°	Concept	1000 cm ²	1 yr
e-ASTROGAM [103]	300 keV - 3 GeV	~2°	Concept	9025 cm ²	1 yr
GECCO [104]	100 keV - 10 MeV	2°	Concept	2000 cm ²	10 ⁶ s

Table II: Summary of properties of the telescopes considered here. Note that for some gamma-ray instruments, we give the performance in the relevant Compton (not pair-production) regime.

the current limits from the number counts of horizontal branch stars and red-giant branch stars in globular clusters [41, 42, 107] (black), the non-observation of photons from the spontaneous decay of axions produced inside SN 1987A (red) [35, 36, 59], anomalous cooling of SN 1987A due to axion emission (cyan) [39], and diffuse gamma-ray background from decays of axions produced inside supernovae (green) [39]. We find that our result for the HB stars in NGC 2808 and NGC 6397 are two orders of magnitude weaker than the current best constraint in the $\mathcal{O}(10)$ keV mass range. On the other hand, for the WR stars in the Quintuplet cluster, we obtain better sensitivity which can cover currently unconstrained ALP parameter space in the 10-100 keV region, probing the ALP-photon coupling down to $g_{a\gamma} \gtrsim 4 \times 10^{-11} \text{ GeV}^{-1}$. Note that the WR stars are roughly an order of magnitude smaller in size compared to the HB stars, although both have similar core temperatures. This allows axions with smaller mean free path to escape the photosphere of WR stars, thus increasing the signal sensitivity, as compared to the HB star case.

We estimated the WR signal detectability for two different initial stellar metallicity: $Z = 0.018$ (blue) and $Z = 0.035$ (cyan). For each stellar model simulated by MESA, we calculate the photon fluence at the Earth, assuming that all 13 WC stars in the Quintuplet cluster follow the same density, temperature, and abundance profiles. By comparing this fluence to the sensitivity of telescopes, we identify the region in the $m_a - g_{a\gamma}$ parameter space that could be probed by the current/future telescopes. These analyses are repeated for all stellar models. Fig. 10 illustrates the mean of $g_{a\gamma}$ bounds and its 1σ uncertainty band for two different metallicity values of $Z = 0.018$ and $Z = 0.035$ with the SPI detector. The uncertainty band accounts for the variation in stellar profile parameters, such as temperature, density, plasma

frequency, etc. The bound itself is derived by requiring that the expected fluence of ALP-induced photon signal in any given pixel of the SPI detector should not exceed the quoted 3σ sensitivity of the detector. We repeated the same exercise for the other telescopes listed in Table II, but the result for SPI turned out to be the best (for reasons mentioned in Sec. III C); therefore, we do not show the sensitivity curves for other telescopes in Fig. 10.

In the regime of large m_a and $g_{a\gamma}$, axion production becomes more efficient, with a greater proportion of axions decaying within the photosphere. On the other hand, in the domain of small m_a and $g_{a\gamma}$, a smaller number of axions is produced while axions have a longer decay length, (i) facilitating them to escape from the star, (ii) making the expected photon signal more diffuse, and (iii) leading to a smaller fraction of axions that have decayed until they reach the Earth. These factors collectively result in distinct shapes in the constrained regions of the parameter space.

The detectability of the axion-induced photon signal also depends on the potential astrophysical backgrounds. A diffuse background of keV-MeV photons could be emitted by several mechanisms. One of the constituents of $\mathcal{O}(\text{MeV})$ gamma-ray background is the decay of a neutral pion produced in astrophysical environments including solar flares, interstellar medium, supernova remnants, molecular clouds, and galaxy clusters [108–110]. Their subsequent decay forms the diffuse gamma-ray background with energies $E_\gamma \simeq m_{\pi^0}/2$. The diffuse $\mathcal{O}(\text{keV})$ photon background is predominantly shaped by thermal emission from white dwarfs, bremsstrahlung, and inverse Compton scattering. Cosmic-ray e^\pm emits photons either by upscattering background low-energy photons (inverse Compton scattering) or traveling in the external electromagnetic fields in which their trajectories are deflected (bremsstrahlung). In this study, we assume the back-

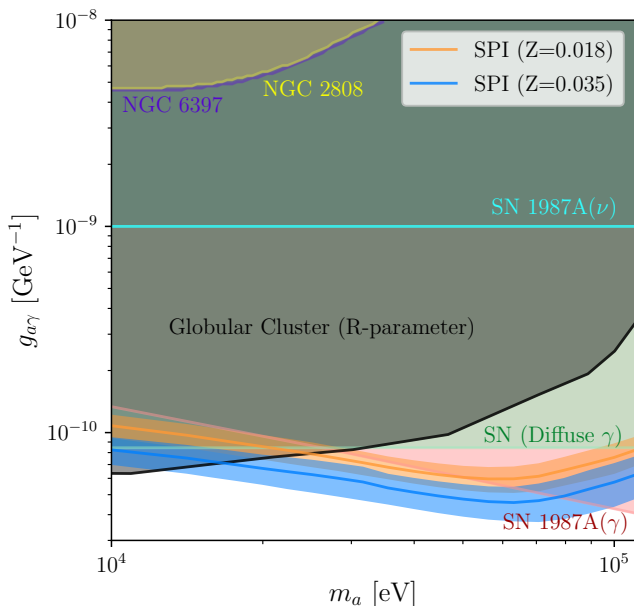


Figure 10: SPI sensitivity of the photon signal induced by decaying ALPs produced from HB stars located in NGC 2808 (yellow) and NGC 6397 (purple), as well as from WR stars located in the Quintuplet cluster for two different metallicity values of $Z = 0.018$ (orange) and $Z = 0.035$ (blue). The existing constraints from R -parameter measurement in globular clusters, SN 1987A and diffuse photon background from supernovae are shown as shaded regions.

ground brightness as described in Ref. [93] to determine the 3σ sensitivity shown in Fig. 10.

As a sanity check, we also made quick estimations on the background $\mathcal{O}(\text{keV})$ and $\mathcal{O}(\text{MeV})$ photon flux as follows: We used `ximage` to obtain the counts of photons at R7 band ($E \in [1.05, 2.04]$ keV) observed by ROSAT [111, 112], and then converted it to the flux by using the `WebPIMMS` [113], confirming that the flux is not high enough to mask the photon signals from decays of axions in this energy band.

Since the size of each pixel in the ROSAT All-Sky Survey diffuse background maps ($12'$) is larger than the angular extension of the Quintuplet cluster ($\sim 1'$), we just choose the one pixel to obtain the photon count rate $1 \times 10^{-4} \text{ s}^{-1}$ from the direction of the cluster. This count rate turns out to be equivalent to the flux $1 \times 10^{-14} \text{ erg/cm}^2/\text{s}$ in the same energy band. In order to obtain the flux, we assume that the HI column density is $2.9 \times 10^{20} \text{ cm}^{-2}$ and the photon spectrum follows the

thermal bremsstrahlung spectrum with $kT = 0.3 \text{ keV}$.

V. DISCUSSION AND CONCLUSION

In this article, we investigated the heavy axion production inside massive stars, such as the WR stars in the Quintuplet cluster and the HB stars in two globular clusters, and the detectability of photons from the ALP decay by current and future X -ray and gamma-ray telescopes. We find that among the existing and planned telescopes in the keV-MeV sensitivity range, the INTEGRAL SPI is best suited for the purpose of the ALP decay-induced photon signal and can probe the axion-photon coupling down to $g_{a\gamma} \gtrsim 4 \times 10^{-11} \text{ GeV}^{-1}$ for axion mass $m_a \sim \mathcal{O}(10 - 100) \text{ keV}$ in the WR star case, surpassing the existing astrophysical constraints by a whisker. On the other hand, our result for the HB star case turns out to be weaker than the existing constraints.

Apart from the uncertainties in the WR star profile and elemental composition, a major source of uncertainty in our result is the initial metallicity of WR stars. Therefore, we showed our results for two different values of the initial metallicity within its uncertainty range ($0.018 \leq Z \leq 0.035$), but found that both metallicity values predict comparable luminosity of ALPs (Fig. 6), and hence, comparable constraints on the axion-photon coupling (Fig. 10).

We have considered only the ALP-photon coupling here for both production and decay of the ALPs. In the presence of other couplings of ALPs to the SM particles (e.g. electrons/nucleons), the production rate would be enhanced, and at the same time, the mean free path would be smaller. However, the ALP decay rate would not change, since for the energy range available inside WR stars (up to a few keV), the ALP is unlikely to decay to other SM particles except photons (and possibly neutrinos, if there is an ALP-neutrino coupling). Therefore, we expect our bounds derived here to remain largely intact.

ACKNOWLEDGMENTS

We thank Alex Chen, Saurav Das, Thomas Gehrman, Mike Nowak, Tekeba Olbemo, and Kuver Sinha for useful discussions and comments on the draft. JB, BD, FF, and TO are partly supported by the U.S. Department of Energy under grant No. DE-SC 0017987. TO is also supported by the University Research Association Visiting Scholars Program.

Appendix A: Models of WR stars

In this section, we explain our code for simulating WR stars by using the MESA stellar evolution code. A sample star is evolved from the pre-MS until near the core-collapse. Firstly, a system is developed up to the point when a radiative core starts to develop with the test suite “20M_pre_ms_to_core.collapse”. Secondly, this star is evolved

until a zero age main sequence (ZAMS) by using a test suite “make_zams_ultra_high_mass”. Lastly, we simulate the evolution of this ZAMS star until near the core-collapse by using a code described below. Parameters in the code are chosen based on Ref. [114], and are summarized in Table III.

We choose the nuclear network `pp_cno_extras_o18_ne22.net`, which includes 26 species: ^1H , ^2H , ^3He , ^4He , ^7Li , ^7Be , ^8B , ^{12}C , ^{13}C , ^{13}N , ^{14}N , ^{15}N , ^{14}O , ^{15}O , ^{16}O , ^{17}O , ^{18}O , ^{17}F , ^{18}F , ^{19}F , ^{18}Ne , ^{19}Ne , ^{20}Ne , ^{22}Ne , ^{22}Mg , ^{24}Mg and reactions involving them. A metallicity, an initial mass, and a rotational velocity at a ZAMS of a sample star are chosen as described in the main text. The observed nitrogen abundance of WNh stars in the Arches cluster prefers the metallicity $Z \in (0.018, 0.035)$, which is anticipated to be close to that of the Quintuplet cluster because both are located near the Galactic Center. We perform simulations for two metallicities $Z = 0.018, 0.035$. For each of these Z values, the hydrogen and helium abundances are determined by the relation $X = 1 - Y - Z$ and Eq. (21), respectively. The relative fractions of metals are set by following Ref. [115]. The initial masses of stars are assumed to follow the Kroupa initial mass function. The probability distribution of initial rotational velocity is described by the Gaussian distribution with a mean velocity $\mu = 100$ km/s and a velocity dispersion $\sigma = 140$ km/s.

The Skye equation of state [116] is selected since it is the most suited equation of state for temperature and density of our interest. Regarding the opacity table, we choose the Type 2 opacity, which allows to simulate the system with time-dependent abundances of carbon and oxygen. The temperature at the stellar surface is calculated by exploiting the Eddington approximation:

$$T^4(\tau) = \frac{3}{4} T_{\text{eff}}^4 \left(\tau + \frac{2}{3} \right), \quad (\text{A1})$$

and the pressure at the surface is obtained by

$$P = \frac{\tau g}{\kappa} \left[1 + P_0 \frac{\kappa L}{\tau M} \frac{1}{6\pi} \right], \quad (\text{A2})$$

where T_{eff} is the effective temperature, M is the stellar mass, L is its luminosity, κ is the opacity, and τ is the optical depth. We have used the Planck units, i.e. $c = 1$ for the speed of light and $G = 1$ for the Newton constant. Note that the second term in Eq. (A2) describes the radiation pressure, which is not negligible for massive stars. We used $P_0 = 2$ in our code.

In massive stars, interactions of photons with ions lead to outward momentum transfer from photons to gas. Consequently, massive stars lose their mass [117]. In order to include this effect, we choose the Dutch scheme as a scheme of winds and set an overall scaling factor $\dot{M} \propto \eta$ as equal to 1. Moreover, a rotation could enhance the mass loss rate of hydrogen burning massive MS stars [118]; the mass loss rate is described by the relation

$$\dot{M}(\Omega) = \dot{M}(0) \left(\frac{1}{1 - \Omega/\Omega_{\text{crit}}} \right)^\xi, \quad (\text{A3})$$

where Ω_{crit} is the critical angular velocity at the surface of a star and $\xi = 0.43$.

We include mixing processes as follows. Convective mixing is incorporated by using the mixing length theory [119] for which we need to choose three parameters: the ratio of a mixing length to a pressure scale height α_{MLT} , a multiplicative factor that determines the mean turbulent speed ν , and the efficiency of convection y . A convective region is located by the Ledoux criterion. A mixing occurring at convective boundaries, an overshoot mixing [120], is dealt with independently. An exponentially decaying overshoot mixing is incorporated at all hydrogen burning, helium burning and metal burning convective boundaries with a factor $f = 0.014$. In addition, we include effects of semiconvection [121] and thermohaline mixing [122]. A semiconvection appears in a region that is thermally unstable but stabilized due to a gradient in composition while thermohaline mixing occurs if a thermally stable region is made unstable due to a gradient in composition. Their diffusion coefficients are proportional to the free parameters α_{sc} and α_{th} . We set $\alpha_{\text{sc}} = 1$ and $\alpha_{\text{th}} = 666$. The rotation of a star induces transports of angular momentum and nuclei. Those transports are approximated by a diffusion process in MESA. We choose parameters that determine the diffusion coefficients as $D_{\text{SH}} = D_{\text{SSI}} = D_{\text{ES}} = D_{\text{GSF}} = D_{\text{ST}} = 1$, $D_{\text{DSI}} = 0$, $f_c = 1/30$, and $f_\mu = 0.05$ by following Ref. [123].

- [1] R. D. Peccei and H. R. Quinn, “CP Conservation in the Presence of Instantons,” *Phys. Rev. Lett.* **38** (1977) 1440–1443.
[2] S. Weinberg, “A New Light Boson?,” *Phys. Rev. Lett.* **40** (1978) 223–226.
[3] F. Wilczek, “Problem of Strong P and T Invariance in the Presence of Instantons,” *Phys. Rev. Lett.* **40** (1978) 279–282.

Parameter	chosen values
nuclear network	pp_cno_extras_o18_ne22.net
initial abundances	Eq. (21), $X = 1 - Y - Z$
fractions of metals	Chosen by following Ref. [115]
initial mass	Kroupa initial mass function
initial surface rotation	Gaussian distribution, $\mu = 100$ km/s, $\sigma = 140$ km/s
equation of state	Skye equation of state
opacity	Type 2
T and P at the surface	Eqs. (A1), (A2), $P_0 = 2$
wind	Dutch scheme, $\eta = 1$
rotational mass loss	Eq. (A3), $\xi = 0.43$
convection	$\alpha_{\text{MLT}} = 2, \nu = 1/3, y = 8$
overshoot	$f_{\text{ov}} = 0.014$
semiconvection	$\alpha_{\text{sc}} = 1$
thermohaline	$\alpha_{\text{th}} = 666$
rotational mixing	$D_{\text{SH}} = D_{\text{SSI}} = D_{\text{ES}} = D_{\text{GSF}} = D_{\text{ST}} = 1, D_{\text{DSI}} = 0, f_c = 1/30, f_\mu = 0.05$

Table III: A summary of the choice of parameters used in our MESA code.

- [4] J. Preskill, M. B. Wise, and F. Wilczek, “Cosmology of the Invisible Axion,” *Phys. Lett. B* **120** (1983) 127–132.
- [5] L. F. Abbott and P. Sikivie, “A Cosmological Bound on the Invisible Axion,” *Phys. Lett. B* **120** (1983) 133–136.
- [6] M. Dine and W. Fischler, “The Not So Harmless Axion,” *Phys. Lett. B* **120** (1983) 137–141.
- [7] P. Svrcek and E. Witten, “Axions In String Theory,” *JHEP* **06** (2006) 051, [[hep-th/0605206](#)].
- [8] A. Arvanitaki, S. Dimopoulos, S. Dubovsky, N. Kaloper, and J. March-Russell, “String Axiverse,” *Phys. Rev. D* **81** (2010) 123530, [[0905.4720](#)].
- [9] K. Choi, S. H. Im, and C. Sub Shin, “Recent Progress in the Physics of Axions and Axion-Like Particles,” *Ann. Rev. Nucl. Part. Sci.* **71** (2021) 225–252, [[2012.05029](#)].
- [10] T. W. Donnelly, S. J. Freedman, R. S. Lytel, R. D. Peccei, and M. Schwartz, “Do Axions Exist?,” *Phys. Rev. D* **18** (1978) 1607.
- [11] J. E. Kim, “Weak Interaction Singlet and Strong CP Invariance,” *Phys. Rev. Lett.* **43** (1979) 103.
- [12] M. A. Shifman, A. I. Vainshtein, and V. I. Zakharov, “Can Confinement Ensure Natural CP Invariance of Strong Interactions?,” *Nucl. Phys. B* **166** (1980) 493–506.
- [13] A. R. Zhitnitsky, “On Possible Suppression of the Axion Hadron Interactions. (In Russian),” *Sov. J. Nucl. Phys.* **31** (1980) 260.
- [14] M. Dine, W. Fischler, and M. Srednicki, “A Simple Solution to the Strong CP Problem with a Harmless Axion,” *Phys. Lett. B* **104** (1981) 199–202.
- [15] V. A. Rubakov, “Grand unification and heavy axion,” *JETP Lett.* **65** (1997) 621–624, [[hep-ph/9703409](#)].
- [16] Z. Berezhiani, L. Gianfagna, and M. Giannotti, “Strong CP problem and mirror world: The Weinberg-Wilczek axion revisited,” *Phys. Lett. B* **500** (2001) 286–296, [[hep-ph/0009290](#)].
- [17] L. Di Luzio, M. Giannotti, E. Nardi, and L. Visinelli, “The landscape of QCD axion models,” *Phys. Rept.* **870** (2020) 1–117, [[2003.01100](#)].
- [18] Y. Nomura and J. Thaler, “Dark Matter through the Axion Portal,” *Phys. Rev. D* **79** (2009) 075008, [[0810.5397](#)].
- [19] D. Cadamuro and J. Redondo, “Cosmological bounds on pseudo Nambu-Goldstone bosons,” *JCAP* **02** (2012) 032, [[1110.2895](#)].
- [20] M. Millea, L. Knox, and B. Fields, “New Bounds for Axions and Axion-Like Particles with keV-GeV Masses,” *Phys. Rev. D* **92** no. 2, (2015) 023010, [[1501.04097](#)].
- [21] P. F. Depta, M. Hufnagel, and K. Schmidt-Hoberg, “Robust cosmological constraints on axion-like particles,” *JCAP* **05** (2020) 009, [[2002.08370](#)].
- [22] J. Jaeckel and M. Spannowsky, “Probing MeV to 90 GeV axion-like particles with LEP and LHC,” *Phys. Lett. B* **753** (2016) 482–487, [[1509.00476](#)].
- [23] **Crystal Ball** Collaboration, D. Antreasyan *et al.*, “Limits on axion and light Higgs boson production in Upsilon (1s) decays,” *Phys. Lett. B* **251** (1990) 204–210.
- [24] **BaBar** Collaboration, B. Aubert *et al.*, “Search for Invisible Decays of a Light Scalar in Radiative Transitions $v_{3S} \rightarrow \gamma A_0$,” in *34th International Conference on High Energy Physics*, 7, 2008. [[0808.0017](#)].
- [25] **Belle-II** Collaboration, F. Abudinén *et al.*, “Search for Axion-Like Particles produced in e^+e^- collisions at Belle II,” *Phys. Rev. Lett.* **125** no. 16, (2020) 161806, [[2007.13071](#)].
- [26] **L3** Collaboration, M. Acciarri *et al.*, “Search for new physics in energetic single photon production in e^+e^- annihilation at the Z resonance,” *Phys. Lett. B* **412** (1997) 201–209.
- [27] **ATLAS** Collaboration, G. Aad *et al.*, “Search for new phenomena in events with at least three photons collected in pp collisions at $\sqrt{s} = 8$ TeV with the ATLAS detector,” *Eur. Phys. J. C* **76** no. 4, (2016) 210, [[1509.05051](#)].
- [28] J. D. Bjorken, S. Ecklund, W. R. Nelson, A. Abashian, C. Church, B. Lu, L. W. Mo, T. A. Nunamaker, and P. Rassmann, “Search for Neutral Metastable Penetrating Particles Produced in the SLAC Beam Dump,” *Phys. Rev. D*

- 38** (1988) 3375.
- [29] M. J. Dolan, T. Ferber, C. Hearty, F. Kahlhoefer, and K. Schmidt-Hoberg, “Revised constraints and Belle II sensitivity for visible and invisible axion-like particles,” *JHEP* **12** (2017) 094, [1709.00009]. [Erratum: JHEP 03, 190 (2021)].
- [30] **CHARM** Collaboration, F. Bergsma *et al.*, “Search for Axion Like Particle Production in 400-GeV Proton - Copper Interactions,” *Phys. Lett. B* **157** (1985) 458–462.
- [31] J. Blumlein *et al.*, “Limits on neutral light scalar and pseudoscalar particles in a proton beam dump experiment,” *Z. Phys. C* **51** (1991) 341–350.
- [32] J. Blumlein *et al.*, “Limits on the mass of light (pseudo)scalar particles from Bethe-Heitler e^+e^- and $\mu^+\mu^-$ pair production in a proton - iron beam dump experiment,” *Int. J. Mod. Phys. A* **7** (1992) 3835–3850.
- [33] E. Masso and R. Toldra, “On a light spinless particle coupled to photons,” *Phys. Rev. D* **52** (1995) 1755–1763, [hep-ph/9503293].
- [34] J. Jaeckel, P. C. Malta, and J. Redondo, “Decay photons from the axionlike particles burst of type II supernovae,” *Phys. Rev. D* **98** no. 5, (2018) 055032, [1702.02964].
- [35] R. Z. Ferreira, M. C. D. Marsh, and E. Müller, “Strong supernovae bounds on ALPs from quantum loops,” *JCAP* **11** (2022) 057, [2205.07896].
- [36] S. Hoof and L. Schulz, “Updated constraints on axion-like particles from temporal information in supernova SN1987A gamma-ray data,” *JCAP* **03** (2023) 054, [2212.09764].
- [37] A. Caputo, G. Raffelt, and E. Vitagliano, “Muonic boson limits: Supernova redux,” *Phys. Rev. D* **105** no. 3, (2022) 035022, [2109.03244].
- [38] E. Müller, P. Carezza, C. Eckner, and A. Goobar, “Constraining MeV-scale axionlike particles with Fermi-LAT observations of SN 2023ixf,” *Phys. Rev. D* **109** no. 2, (2024) 023018, [2306.16397].
- [39] A. Caputo, H.-T. Janka, G. Raffelt, and E. Vitagliano, “Low-Energy Supernovae Severely Constrain Radiative Particle Decays,” *Phys. Rev. Lett.* **128** no. 22, (2022) 221103, [2201.09890].
- [40] N. H. Nguyen, E. H. Tanin, and M. Kamionkowski, “Spectra of axions emitted from main sequence stars,” *JCAP* **11** (2023) 091, [2307.11216].
- [41] A. Ayala, I. Domínguez, M. Giannotti, A. Mirizzi, and O. Straniero, “Revisiting the bound on axion-photon coupling from Globular Clusters,” *Phys. Rev. Lett.* **113** no. 19, (2014) 191302, [1406.6053].
- [42] P. Carezza, O. Straniero, B. Döbrich, M. Giannotti, G. Lucente, and A. Mirizzi, “Constraints on the coupling with photons of heavy axion-like-particles from Globular Clusters,” *Phys. Lett. B* **809** (2020) 135709, [2004.08399].
- [43] M. J. Dolan, F. J. Hiskens, and R. R. Volkas, “Advancing globular cluster constraints on the axion-photon coupling,” *JCAP* **10** (2022) 096, [2207.03102].
- [44] C. Dessert, J. W. Foster, and B. R. Safdi, “X-ray Searches for Axions from Super Star Clusters,” *Phys. Rev. Lett.* **125** no. 26, (2020) 261102, [2008.03305].
- [45] B. Berenji, J. Gaskins, and M. Meyer, “Constraints on Axions and Axionlike Particles from Fermi Large Area Telescope Observations of Neutron Stars,” *Phys. Rev. D* **93** no. 4, (2016) 045019, [1602.00091].
- [46] P. S. B. Dev, J.-F. Fortin, S. P. Harris, K. Sinha, and Y. Zhang, “First Constraints on the Photon Coupling of Axionlike Particles from Multimessenger Studies of the Neutron Star Merger GW170817,” *Phys. Rev. Lett.* **132** no. 10, (2024) 101003, [2305.01002].
- [47] M. Diamond, D. F. G. Fiorillo, G. Marques-Tavares, I. Tamborra, and E. Vitagliano, “Multimessenger Constraints on Radiatively Decaying Axions from GW170817,” *Phys. Rev. Lett.* **132** no. 10, (2024) 101004, [2305.10327].
- [48] D. C. Abbott and P. S. Conti, “Wolf-rayet stars,” *Ann. Rev. Astron. Astrophys.* **25** (Jan., 1987) 113–150.
- [49] H. Primakoff, “Photoproduction of neutral mesons in nuclear electric fields and the mean life of the neutral meson,” *Phys. Rev.* **81** (1951) 899.
- [50] L. Di Lella, A. Pilaftsis, G. Raffelt, and K. Zioutas, “Search for solar Kaluza-Klein axions in theories of low scale quantum gravity,” *Phys. Rev. D* **62** (2000) 125011, [hep-ph/0006327].
- [51] M. Bastero-Gil, C. Beaufort, and D. Santos, “Solar axions in large extra dimensions,” *JCAP* **10** (2021) 048, [2107.13337].
- [52] G. G. Raffelt, “ASTROPHYSICAL AXION BOUNDS DIMINISHED BY SCREENING EFFECTS,” *Phys. Rev. D* **33** (1986) 897.
- [53] S. J. Brodsky, E. Mottola, I. J. Muzinich, and M. Soldate, “LASER INDUCED AXION PHOTOPRODUCTION,” *Phys. Rev. Lett.* **56** (1986) 1763. [Erratum: Phys.Rev.Lett. 57, 502 (1986)].
- [54] G. G. Raffelt, “Plasmon Decay Into Low Mass Bosons in Stars,” *Phys. Rev. D* **37** (1988) 1356.
- [55] G. G. Raffelt, “Astrophysical methods to constrain axions and other novel particle phenomena,” *Phys. Rept.* **198** (1990) 1–113.
- [56] D. Cadamuro, S. Hannestad, G. Raffelt, and J. Redondo, “Cosmological bounds on sub-MeV mass axions,” *JCAP* **02** (2011) 003, [1011.3694].
- [57] A. Payez, C. Evoli, T. Fischer, M. Giannotti, A. Mirizzi, and A. Ringwald, “Revisiting the SN1987A gamma-ray limit on ultralight axion-like particles,” *JCAP* **02** (2015) 006, [1410.3747].
- [58] A. J. Millar, S. Baum, M. Lawson, and M. C. D. Marsh, “Axion-photon conversion in strongly magnetised plasmas,” *JCAP* **11** (2021) 013, [2107.07399].
- [59] E. Müller, F. Calore, P. Carezza, C. Eckner, and M. C. D. Marsh, “Investigating the gamma-ray burst from decaying MeV-scale axion-like particles produced in supernova explosions,” *JCAP* **07** (2023) 056, [2304.01060].
- [60] H. A. Weldon, “Covariant Calculations at Finite Temperature: The Relativistic Plasma,” *Phys. Rev. D* **26** (1982) 1394.
- [61] H. A. Weldon, “Simple Rules for Discontinuities in Finite Temperature Field Theory,” *Phys. Rev. D* **28** (1983) 2007.

- [62] T. Altherr, “Axion Emission From a Hot Plasma,” *Z. Phys. C* **47** (1990) 559–564.
- [63] T. Altherr and U. Kraemmer, “Gauge field theory methods for ultradegenerate and ultrarelativistic plasmas,” *Astropart. Phys.* **1** (1992) 133–158.
- [64] T. Altherr, E. Petitgirard, and T. del Rio Gaztelurrutia, “Axion emission from red giants and white dwarfs,” *Astropart. Phys.* **2** (1994) 175–186, [[hep-ph/9310304](#)].
- [65] E. Braaten and D. Segel, “Neutrino energy loss from the plasma process at all temperatures and densities,” *Phys. Rev. D* **48** (1993) 1478–1491, [[hep-ph/9302213](#)].
- [66] J. I. Kapusta and C. Gale, *Finite-temperature field theory: Principles and applications*. Cambridge Monographs on Mathematical Physics. Cambridge University Press, 2011.
- [67] H. An, M. Pospelov, and J. Pradler, “New stellar constraints on dark photons,” *Phys. Lett. B* **725** (2013) 190–195, [[1302.3884](#)].
- [68] MESA Collaboration, B. Paxton, L. Bildsten, A. Dotter, F. Herwig, P. Lesaffre, and F. Timmes, “Modules for Experiments in Stellar Astrophysics (MESA),” *Astrophys. J. Suppl.* **192** (2011) 3, [[1009.1622](#)].
- [69] B. Paxton *et al.*, “Modules for Experiments in Stellar Astrophysics (MESA): Planets, Oscillations, Rotation, and Massive Stars,” *Astrophys. J. Suppl.* **208** (2013) 4, [[1301.0319](#)].
- [70] B. Paxton *et al.*, “Modules for Experiments in Stellar Astrophysics (MESA): Binaries, Pulsations, and Explosions,” *Astrophys. J. Suppl.* **220** no. 1, (2015) 15, [[1506.03146](#)].
- [71] B. Paxton *et al.*, “Modules for Experiments in Stellar Astrophysics (MESA): Convective Boundaries, Element Diffusion, and Massive Star Explosions,” *Astrophys. J. Suppl.* **234** no. 2, (2018) 34, [[1710.08424](#)].
- [72] B. Paxton *et al.*, “Modules for Experiments in Stellar Astrophysics (MESA): Pulsating Variable Stars, Rotation, Convective Boundaries, and Energy Conservation,” *Astrophys. J. Suppl.* **243** no. 1, (2019) 10, [[1903.01426](#)].
- [73] P. A. Crowther, “Physical Properties of Wolf-Rayet Stars,” *Ann. Rev. Astron. Astrophys.* **45** no. 1, (Sept., 2007) 177–219, [[astro-ph/0610356](#)].
- [74] W. E. Harris, “A Catalog of Parameters for Globular Clusters in the Milky Way,” *Astrophys. J.* **112** (Oct., 1996) 1487.
- [75] W. E. Harris, “A New Catalog of Globular Clusters in the Milky Way,” *arXiv e-prints* (Dec., 2010) arXiv:1012.3224, [[1012.3224](#)].
- [76] W. E. Harris, G. L. H. Harris, and M. Alessi, “A Catalog of Globular Cluster Systems: What Determines the Size of a Galaxy’s Globular Cluster Population?,” *Astrophys. J.* **772** no. 2, (Aug., 2013) 82, [[1306.2247](#)].
- [77] J. Boyles, D. R. Lorimer, P. J. Turk, R. Mnatsakanov, R. S. Lynch, S. M. Ransom, P. C. Freire, and K. Belczynski, “Young Radio Pulsars in Galactic Globular Clusters,” *Astrophys. J.* **742** no. 1, (Nov., 2011) 51, [[1108.4402](#)].
- [78] T. Constantino, S. W. Campbell, and J. C. Lattanzio, “The treatment of mixing in core helium-burning models - III. Suppressing core breathing pulses with a new constraint on overshoot,” *Mon. Not. Roy. Astron. Soc.* **472** no. 4, (Dec., 2017) 4900–4909, [[1709.06381](#)].
- [79] E. L. Sandquist, “A catalogue of helium abundance indicators from globular cluster photometry,” *Mon. Not. Roy. Astron. Soc.* **313** no. 3, (Apr., 2000) 571–586, [[astro-ph/9911237](#)].
- [80] J. S. Clark, M. E. Lohr, L. R. Patrick, F. Najarro, H. Dong, and D. F. Figer, “An updated stellar census of the Quintuplet cluster,” *Astron. Astrophys.* **618** (Oct., 2018) A2, [[1805.10139](#)].
- [81] Planck Collaboration, N. Aghanim *et al.*, “Planck 2018 results. VI. Cosmological parameters,” *Astron. Astrophys.* **641** (2020) A6, [[1807.06209](#)]. [Erratum: *Astron. Astrophys.* 652, C4 (2021)].
- [82] M. Asplund, N. Grevesse, A. J. Sauval, and P. Scott, “The Chemical Composition of the Sun,” *Ann. Rev. Astron. Astrophys.* **47** no. 1, (Sept., 2009) 481–522, [[0909.0948](#)].
- [83] M. J. Reid, “The distance to the center of the Galaxy,” *Ann. Rev. Astron. Astrophys.* **31** (Jan., 1993) 345–372.
- [84] P. Kroupa, “On the variation of the initial mass function,” *Mon. Not. Roy. Astron. Soc.* **322** no. 2, (Apr., 2001) 231–246, [[astro-ph/0009005](#)].
- [85] I. Hunter, D. J. Lennon, P. L. Dufton, C. Trundle, S. Simon-Diaz, S. J. Smartt, R. S. I. Ryans, and C. J. Evans, “The VLT-FLAMES survey of massive stars: Atmospheric parameters and rotational velocity distributions for B-type stars in the Magellanic Clouds,” *Astron. Astrophys.* **479** (2008) 541, [[0711.2264](#)].
- [86] I. Brott, C. J. Evans, I. Hunter, A. de Koter, N. Langer, P. L. Dufton, M. Cantiello, C. Trundle, D. J. Lennon, S. E. de Mink, S. C. Yoon, and P. Anders, “Rotating massive main-sequence stars. II. Simulating a population of LMC early B-type stars as a test of rotational mixing,” *Astron. Astrophys.* **530** (June, 2011) A116, [[1102.0766](#)].
- [87] S. Balaji, P. S. B. Dev, J. Silk, and Y. Zhang, “Improved stellar limits on a light CP-even scalar,” *JCAP* **12** (2022) 024, [[2205.01669](#)].
- [88] A. H. Jaffe and M. S. Turner, “Gamma-rays and the decay of neutrinos from SN1987A,” *Phys. Rev. D* **55** (1997) 7951–7959, [[astro-ph/9601104](#)].
- [89] XMM Collaboration, F. Jansen *et al.*, “XMM-Newton observatory. I. The spacecraft and operations,” *Astron. Astrophys.* **365** (2001) L1–L6.
- [90] NuSTAR Collaboration, F. A. Harrison *et al.*, “The Nuclear Spectroscopic Telescope Array (NuSTAR) High-Energy X-Ray Mission,” *Astrophys. J.* **770** (2013) 103, [[1301.7307](#)].
- [91] F. Lebrun *et al.*, “ISGRI: The Integral Soft Gamma-Ray Imager,” *Astron. Astrophys.* **411** (2003) L141–L148, [[astro-ph/0310362](#)].
- [92] G. Di Cocco *et al.*, “Ibis/picisit in-flight performances,” *Astron. Astrophys.* **411** (2003) L189–L196, [[astro-ph/0309224](#)].
- [93] G. Vedrenne *et al.*, “SPI: The spectrometer aboard INTEGRAL,” *Astron. Astrophys.* **411** (Nov., 2003) L63–L70.
- [94] N. Lund *et al.*, “JEM-X: The X-ray monitor aboard INTEGRAL,” *Astron. Astrophys.* **411** (Nov., 2003) L231–L238.
- [95] SWIFT Collaboration, D. N. Burrows *et al.*, “The Swift X-ray Telescope,” *Space Sci. Rev.* **120** (2005) 165,

- [astro-ph/0508071].
- [96] **eROSITA** Collaboration, A. Merloni *et al.*, “eROSITA Science Book: Mapping the Structure of the Energetic Universe,” [1209.3114].
- [97] **Insight-HXMT Team** Collaboration, S.-N. Zhang *et al.*, “Overview to the Hard X-ray Modulation Telescope (*Insight-HXMT*) Satellite,” *Sci. China Phys. Mech. Astron.* **63** no. 4, (2020) 249502, [1910.09613].
- [98] J. A. Tomsick *et al.*, “The Compton Spectrometer and Imager,” *PoS ICRC2023* (2023) 745, [2308.12362].
- [99] **AMEGO** Collaboration, R. Caputo *et al.*, “All-sky Medium Energy Gamma-ray Observatory: Exploring the Extreme Multimessenger Universe,” [1907.07558].
- [100] R. Caputo *et al.*, “All-sky Medium Energy Gamma-ray Observatory eXplorer mission concept,” *J. Astron. Telesc. Instrum. Syst.* **8** no. 4, (2022) 044003, [2208.04990].
- [101] **APT** Collaboration, J. H. Buckley *et al.*, “The Advanced Particle-astrophysics Telescope (APT) Project Status,” *PoS ICRC2021* (2021) 655.
- [102] A. De Angelis *et al.*, “Gamma-ray astrophysics in the MeV range: The ASTROGAM concept and beyond,” *Exper. Astron.* **51** no. 3, (2021) 1225–1254, [2102.02460].
- [103] **e-ASTROGAM** Collaboration, M. Tavani *et al.*, “Science with e-ASTROGAM: A space mission for MeV–GeV gamma-ray astrophysics,” *JHEAp* **19** (2018) 1–106, [1711.01265].
- [104] E. Orlando *et al.*, “Exploring the MeV sky with a combined coded mask and Compton telescope: the Galactic Explorer with a Coded aperture mask Compton telescope (GECCO),” *JCAP* **07** no. 07, (2022) 036, [2112.07190].
- [105] **e-ASTROGAM** Collaboration, R. Rando, A. De Angelis, and M. Mallamaci, “e-ASTROGAM: a space mission for MeV–GeV gamma-ray astrophysics,” *J. Phys. Conf. Ser.* **1181** no. 1, (2019) 012044.
- [106] G. Lucchetta, M. Ackermann, D. Berge, and R. Bühler, “Introducing the MeVCube concept: a CubeSat for MeV observations,” *JCAP* **08** no. 08, (2022) 013, [2204.01325].
- [107] G. Lucente, O. Straniero, P. Carena, M. Giannotti, and A. Mirizzi, “Constraining Heavy Axionlike Particles by Energy Deposition in Globular Cluster Stars,” *Phys. Rev. Lett.* **129** no. 1, (2022) 011101, [2203.01336].
- [108] R. J. Murphy, C. D. Dermer, and R. Ramaty, “High-Energy Processes in Solar Flares,” *Astrophys. J. Suppl.* **63** (Mar., 1987) 721.
- [109] C. Pfrommer and T. A. Enßlin, “Constraining the population of cosmic ray protons in cooling flow clusters with γ -ray and radio observations: Are radio mini-halos of hadronic origin?,” *Astron. Astrophys.* **413** (Jan., 2004) 17–36.
- [110] Y. Ohira, K. Kohri, and N. Kawanaka, “Positron annihilation as a cosmic ray probe,” *Mon. Not. Roy. Astron. Soc.* **421** no. 1, (Mar., 2012) L102–L106, [1103.4140].
- [111] S. L. Snowden, M. J. Freyberg, P. P. Plucinsky, J. H. M. M. Schmitt, J. Truemper, W. Voges, R. J. Edgar, D. McCammon, and W. T. Sanders, “First Maps of the Soft X-Ray Diffuse Background from the ROSAT XRT/PSPC All-Sky Survey,” *Astrophys. J.* **454** (Dec., 1995) 643.
- [112] S. L. Snowden, R. Egger, M. J. Freyberg, D. McCammon, P. P. Plucinsky, W. T. Sanders, J. H. M. M. Schmitt, J. Trümper, and W. Voges, “ROSAT Survey Diffuse X-Ray Background Maps. II.,” *Astrophys. J.* **485** no. 1, (Aug., 1997) 125–135.
- [113] S. L. Snowden, D. McCammon, D. N. Burrows, and J. A. Mendenhall, “Analysis Procedures for ROSAT XRT/PSPC Observations of Extended Objects and the Diffuse Background,” *Astrophys. J.* **424** (Apr., 1994) 714.
- [114] J. Choi, A. Dotter, C. Conroy, M. Cantiello, B. Paxton, and B. D. Johnson, “Mesa Isochrones and Stellar Tracks (MIST). I. Solar-scaled Models,” *Astrophys. J.* **823** no. 2, (June, 2016) 102, [1604.08592].
- [115] N. Grevesse and A. J. Sauval, “Standard Solar Composition,” *Space Sci. Rev.* **85** (1998) 161–174.
- [116] A. S. Jermyn, J. Schwab, E. Bauer, F. X. Timmes, and A. Y. Potekhin, “Skye: A Differentiable Equation of State,” *Astrophys. J.* **913** no. 1, (May, 2021) 72, [2104.00691].
- [117] J. S. Vink, A. de Koter, and H. J. G. L. M. Lamers, “Mass-loss predictions for o and b stars as a function of metallicity,” *Astron. Astrophys.* **369** (2001) 574–588, [astro-ph/0101509].
- [118] N. Langer, “Coupled mass and angular momentum loss of massive main sequence stars,” *Astron. Astrophys.* **329** (Jan., 1998) 551–558.
- [119] L. Henyey, M. S. Vardya, and P. Bodenheimer, “Studies in Stellar Evolution. III. The Calculation of Model Envelopes.,” *Astrophys. J.* **142** (Oct., 1965) 841.
- [120] F. Herwig, “The evolution of agb stars with convective overshoot,” *Astron. Astrophys.* **360** (2000) 952–968, [astro-ph/0007139].
- [121] N. Langer, K. J. Fricke, and D. Sugimoto, “Semiconvective diffusion and energy transport,” *Astron. Astrophys.* **126** no. 1, (Sept., 1983) 207.
- [122] R. Kippenhahn, G. Ruschenplatt, and H. C. Thomas, “The time scale of thermohaline mixing in stars,” *Astron. Astrophys.* **91** no. 1-2, (Nov., 1980) 175–180.
- [123] A. Heger, N. Langer, and S. E. Woosley, “Presupernova Evolution of Rotating Massive Stars. I. Numerical Method and Evolution of the Internal Stellar Structure,” *Astrophys. J.* **528** no. 1, (Jan., 2000) 368–396, [astro-ph/9904132].